bioRxiv preprint doi: https://doi.org/10.1101/2022.11.07.515476; this version posted November 7, 2022. The copyright holder for this preprint (which was not certified by peer review) is the author/funder. All rights reserved. No reuse allowed without permission.

Kinetochore microtubules flux poleward along fixed centrosome-anchored microtubules during the metaphase of *C. elegans* one-cell embryo.

Nina Soler[1], Laurent Chesneau[1], Hélène Bouvrais[1], Sylvain Pastezeur[1], Loïc Le Marrec[2], Jacques Pecreaux[1]

[1] CNRS, Univ Rennes, IGDR (Institut de Génétique et Développement de Rennes) – UMR 6290, F-35000 Rennes, France.

[2] CNRS, Univ Rennes, IRMAR (Institut de Recherche Mathématique de Rennes) – UMR 6625, F-35000 Rennes, France.

nina.soler.1@univ-rennes1.fr

jacques.pecreaux@univ-rennes1.fr

Abstract:

The microtubule array, assembled into the mitotic spindle, polymerises from the centrosomes and the chromosomes in many organisms. Their plus ends alternate between growing and shrinking. This dynamic instability plays a key role in pulling on the kinetochores to check the spindle assembly and correct the errors in chromosome attachments. In addition, the minus ends at centrosomes can undergo depolymerisation coordinated with the polymerisation of the plus ends at the kinetochores. Such a mechanism, among others, creates treadmilling, *id est* a net poleward movement of microtubules called poleward flux. This flux is involved in many roles, chromosome congression in prometaphase, chromosome misattachment detection and correction, spindle length maintenance in metaphase, and synchronous segregation of sister chromatids in anaphase. Interestingly, no poleward flux was measured in the *Caenorhabditis elegans* single-cell embryo, despite it is equipped with all homologous proteins involved in this mechanism in other organisms. To investigate this peculiarity, we labelled the microtubules and photobleached them in a rectangular region. Surprisingly, we observed that both edges of the bleached zone (fronts) move inwards, closing the dark area. However, the middle of the bleached zone does not move clearly, confirming the absence of a global poleward flow. The dynamics of the microtubules emanating from the centrosomes combined with the diffraction due to microscopy imaging account for the apparent movement of the front on the centrosome side. Therefore, we suggest no flux of the centrosome-anchored (spindle) microtubules. In contrast, on the chromosome side, we observed a front moving poleward, faster than the one on the other side, and dependent on proteins ensuring the attachment and growth of microtubules at kinetochores, NDC-80, CLS-2^{CLASP}, and ZYG-9^{XMAP215}. Besides, we found that the depletion of the depolymerase KLP-7^{MCAK} does not impair this poleward recovery. Finally, the faster recovery is restricted to the spindle region close to the chromosomes. Therefore, we suggest that the kinetochore microtubules undergo a poleward flux, moving with respect to spindle microtubules. Because the kinetochore microtubules are shorter than the half-spindle, this flux is localised close to the chromosomes. Furthermore, it may not rely on

bioRxiv preprint doi: https://doi.org/10.1101/2022.11.07.515476; this version posted November 7, 2022. The copyright holder for this preprint (which was not certified by peer review) is the author/funder. All rights reserved. No reuse allowed without permission.

treadmilling as KLP-7^{MCAK} is dispensable. This spatially restricted flux found in the nematode may be related to the slow elongation of the spindle during metaphase and may buffer the strong pulling forces exerted by the cortical force generators at the spindle poles.

INTRODUCTION

During cell division, the mitotic spindle ensures a faithful partitioning of the genetic material into two identical sets distributed to each daughter cell. This specialised structure is assembled from microtubules (MTs) and their associated proteins (MAPs), especially molecular motors and cross-linkers. The microtubules are semi-flexible polymers assembled from dimers of α- and β-tubulin, making them polarised. They alternate growth and shrinkage, and their plus ends are more dynamic than their minus ends (Akhmanova and Steinmetz, 2015). In the nematode *C. elegans* zygote, we distinguish two populations of microtubules in the spindle according to where their extremities are anchored: kinetochore microtubules (kMT) whose plus-ends are localised at the chromosomes while minus-ends distribute along the spindle; spindle microtubules (sMT) whose minus-ends at the centrosomes and along the microtubules' lattice create a branched network (Muller-Reichert et al., 2010; Redemann et al., 2017), while their plus-ends does not contact the kinetochore. Dynamic instability is essential for the spindle functions (Vicente and Wordeman, 2019), a feature largely used in cancer therapies (Steinmetz and Prota, 2018; Wordeman and Vicente, 2021). Therefore, numerous MAPs ensure a precise regulation of microtubule dynamics along the various phases of mitosis (Lacroix et al., 2018; Srayko et al., 2005). These molecular motors and MAPs stochastically bind and unbind to the microtubules, making the spindle highly dynamic (Elting et al., 2018; Nazockdast and Redemann, 2020).

An important aspect of ensuring spindle function is the attachment of the chromosomes by the kMT while preserving microtubule plus-end dynamic instability (Bakhoum and Compton, 2012). Thus, a specialised structure assembles at the centromeric regions of the chromosomes: the kinetochore (Cheeseman, 2014; Musacchio and Desai, 2017). In particular, the outer kinetochore protein NDC-80 makes the bridge with the microtubules. In the nematode, chromosomes are holocentric; thus, kinetochores are scattered all along the chromosomes (Maddox et al., 2004). Chromosome attachment happens firstly along the lattice of the microtubules (side-on) before being converted into an attachment at their plus-end (end-on) (Cheerambathur et al., 2013; Magidson et al., 2011). Importantly, it enables the microtubule plus-ends to alternate growth and shrinkage, keeping the chromosome attached. It can also withstand the tension exerted on the kinetochore by the microtubules. Indeed, this tension is needed both for the spindle assembly checkpoint (SAC) to detect chromosome misattachment, and for correcting these errors (Kuhn and Dumont, 2019; McVey et al., 2021). NDC-80 and its complex are essential for such an end-on MT-kinetochore coupling (Cheeseman et al., 2004; Suzuki et al., 2016; Ye et al., 2016). Other MAPs regulate the dynamics of the attached microtubule as the rescue factor CLS-2^{CLASP} (Al-Bassam and Chang, 2011; Cheeseman et al., 2005; Matthews et al., 1998). Some ubiquitous regulators also contribute, such as the polymerisation enhancer ZYG-9^{XMAP215} (Matthews et al., 1998). Importantly, in the nematode, like in other organisms, only a quarter of the kMTs are long enough to directly reach the spindle pole (Kiewisz et al., 2022; Petry, 2016; Redemann et al., 2017). The remaining kMTs are likely coupled to sMTs. While such a kinetochore assembly is similar to other organisms and the involved proteins are long known to be homologous (Oegema and Hyman, 2006; Pintard and Bowerman, 2019), the SAC is weak in the *C. elegans* zygote, and some of its components are dispensable (Gerhold et al., 2018; Tarailo et al., 2007).

bioRxiv preprint doi: https://doi.org/10.1101/2022.11.07.515476; this version posted November 7, 2022. The copyright holder for this preprint (which was not certified by peer review) is the author/funder. All rights reserved. No reuse allowed without permission.

The process of capturing and attaching chromosomes is partly stochastic, leaving a possibility for errors. These are usually intercepted by the SAC (Nicklas, 1997). Keeping the microtubule dynamics appears of utmost importance to maintain the kinetochore under tension while microtubules are polymerising (Bakhoum et al., 2009; Cimini et al., 2006; Lampson and Grishchuk, 2017). Such dynamics combined with minus-ends dynamics lead to poleward flux (O'Toole et al., 2003). Reportedly, it creates a solid displacement of the microtubule network away from chromosomes (Barisic et al., 2021; Hotani and Horio, 1988; Mitchison, 1989; Steblyanko et al., 2020; Waters et al., 1996). A poleward flux was measured in various organisms, from Xenopus to mammals (Brust-Mascher et al., 2004; Brust-Mascher et al., 2009; Maddox et al., 2002; Maddox et al., 2003; Maiato et al., 2005; Matos et al., 2009; Yang et al., 2008). It plays an important role in correcting chromosome attachment errors, putatively by renewing the microtubules in contact with the kinetochore (Ganem et al., 2005; Matos et al., 2009; Pereira and Maiato, 2012). During anaphase A, it also contributes to a synchronous migration of the sister chromatids toward their facing spindle pole (Ganem et al., 2005; Matos et al., 2009; Mitchison and Salmon, 1992). The most obvious flux mechanism is treadmilling, where the microtubule grows on the kinetochore side coordinatedly with shortening at the spindle pole. This latter part would power the mechanism (Gaetz and Kapoor, 2004; Ganem et al., 2005). Such a mechanism was also recreated *in vitro* following a minimal system approach with only four proteins, XMAP215^{ZYG-9}, the microtubule plus-end binding EB1^{EBP-2}, CLASP2^{CLS-2}, and the microtubule depolymerising kinesin MCAK^{KLP-7} (Arpag et al., 2020). This latter kinesin is essential to depolymerise the microtubules on the centrosome side. It can be assisted by severing enzymes like katanin, spastin and fidgetin (Zhang et al., 2007). Furthermore, treadmilling is plainly consistent with the gel-like behaviour of the spindle (Dalton et al., 2022) and the classic flux measurements using photobleaching/photoconversion experiments (Barisic et al., 2021; Mitchison and Salmon, 1992). They all suggest a mostly solid motion of the spindle microtubule network at steady state. The proposed alternative flux mechanisms are twofold. Firstly, the sliding of overlapping antiparallel microtubules by specialised molecular motors, kinesin-5^{BMK-1} and kinesin-12 KIF15^{KLP-18} (Miyamoto et al., 2004; Steblyanko et al., 2020; Uteng et al., 2008), although this latter seems more specialised into parallel microtubules (Drechsler and McAinsh, 2016). Variants were proposed by sliding bridging fibres along each other (Jagric et al., 2021). The motion of these fibres is transmitted to other microtubules, including kMT and sMTs, by cross-linking agents or motors like HSET$^{KLP-15/16/17}$, NuMA^{LIN-5} or PRC1^{SPD-1} (Elting et al., 2014; Risteski et al., 2022; Steblyanko et al., 2020). Secondly, chromokinesin KIF4A^{KLP-19} congresses the chromosome arms and generates a reaction force that pushes the kMTs away from the chromosomes (Steblyanko et al., 2020; Wandke et al., 2012). Overall, these various mechanisms can also superimpose to ensure a robust movement of the microtubules poleward.

Surprisingly, in the nematode C. e*legans,* no flux was reported in anaphase, while a putative but weak anti-poleward flux was suggested at metaphase (Labbe et al., 2004; Redemann et al., 2017). It is noteworthy that microtubules are highly dynamic in the nematode due to tubulin specificities (Chaaban et al., 2018). In contrast, a flux was found in meiosis (Lantzsch et al., 2021). These paradoxes led us to investigate the flux during mitotic metaphase using the established fluorescence recovery after photobleaching (FRAP) (Axelrod et al., 1976; Giakoumakis et al., 2017; Matsuda and Nagai, 2014; White and Stelzer, 1999). Whereas we found no net flux for the spindle as a whole, we observed an apparent anti-poleward microtubule flux close to the centrosomes. We also measured a poleward displacement of the microtubules close to the chromosomes. Distinct mechanisms correspond to each of these two motions. We suggest that microtubule dynamics account for the apparent anti-poleward motion of sMTs while kMTs flux poleward along sMTs. Nevertheless, the extent of the kMTs is shorter than a half-spindle, so it prevents seeing this flux far from the kinetochore.

bioRxiv preprint doi: https://doi.org/10.1101/2022.11.07.515476; this version posted November 7, 2022. The copyright holder for this preprint (which was not certified by peer review) is the author/funder. All rights reserved. No reuse allowed without permission.

RESULTS

Two distinct microtubule-dynamics mechanisms recover fluorescence after FRAP.

We set out to investigate the dynamics of the microtubules within the metaphasic spindle using FRAP. We imaged the metaphasic spindle of the *C. elegans* zygote using GFP::TBB-2$^{\beta\text{-tubulin}}$. We previously used this strain and detected no phenotype (Bouvrais et al., 2021). During metaphase, we bleached the fluorescently-labelled tubulin in a band-shaped region, 2.6 µm-wide, perpendicular to the spindle axis and covering the spindle but extending up to the cytoplasm (Fig 1A). The proximal boundary of the bleached area was between 0.5 and 2 µm away from the chromosomes (defined as the area devoid of microtubules). Since the spindle is moving and slowly elongating during metaphase, we performed an intensity-based registration of the images, over time, using the icy software (de Chaumont et al., 2012). We used the centrosome on the bleaching side as a spatial reference (see Methods § Averaging kymograph over several embryos, Fig 1A). We monitored the fluorescence recovery over time and fitted it assuming a single microtubule population, thus with a single exponential, over a 60 s range during metaphase (Giakoumakis et al., 2017; Girao and Maiato, 2020) (see methods § Imaging conditions). We used a global fitting approach to safeguard against variability between embryos and obtained the confidence interval by thresholding the empirical likelihood (Bouvrais et al., 2021). In doing so, we imposed the same model parameters on each embryo of a given data set but maximised the product of the embryo-wise likelihoods (Beechem, 1992). We found a recovery half-time inside the spindle about three times longer than in the cytoplasm, although the recovery was never complete (Fig 1D). The spindle half-life was consistent with previous measurements (Redemann et al., 2017) and suggested that free fluorescent tubulin is available within seconds within the spindle. Therefore, dimer diffusion did not account for most of the recovery inside the spindle.

The flux of microtubules classically accounts for recovery in the spindle. However, to our knowledge, it was only tested once during nematode mitotic metaphase, and a very weak anti-poleward flux was found (Redemann et al., 2017). We performed photobleaching within the posterior half-spindle with an area different from above (Fig 1B) and generated a kymograph of the microtubule density (fluorescence) along the spindle axis. We again registered the images over time and then segmented the bleached area (Fig 1C, S8, see methods § Imaging condition for photobleaching). We then monitored the displacement of the mid-curve between the two edges over time and extracted its slope by linear fitting (Fig 1H). The value reads 0.017 ± 0.028 µm/s and oriented poleward (N = 10, mean ± standard error (se) obtained by Jackknife resampling, p = 0.56 compared to 0, see methods § Automatic recognition of the bleached region border). We concluded to no significant flux. It is consistent with the previous reports on the lack of flux in metaphase and anaphase (Labbe et al., 2004; Redemann et al., 2017). However, a visual inspection of the kymograph (Fig 1CH) indicated a recovery by closing the bleached area through two inward-oriented fronts.

We investigated this V-shaped recovery and set out to measure the closure velocities. We produced the kymograph along the spindle axis and median-projected along the transverse axis (Fig S1, methods § Assembling a homogenous set *et seq.*). The fast dynamics of the microtubules imposed imaging at 12.5 frames per second, leading to a low signal-to-noise ratio (SNR). We then aligned the kymographs from several embryos on the centrosome-side corner of the bleached region corresponding to the first bleached image. We averaged the kymograph between embryos after matching the intensity histograms for each embryo. We then segmented the bleached region of the averaged kymograph and fitted its boundaries with lines (Fig 1H). We used a leave-one-out resampling (Jackknife) to obtain the standard errors of the region-edge slopes (Efron and Tibshirani, 1993; Quenouille, 1956). Such an approach also enabled us to visualise the front-slope

bioRxiv preprint doi: https://doi.org/10.1101/2022.11.07.515476; this version posted November 7, 2022. The copyright holder for this preprint (which was not certified by peer review) is the author/funder. All rights reserved. No reuse allowed without permission.

distribution by displaying N-1 averages (Fig 1F, Methods § Statistics on kymograph front slopes). We measured 0.117 ± 0.028 μm/s on the chromosome side, which significantly differed from 0 (N = 10, p = 0.002) and 0.082 ± 0.039 on the centrosome side (p = 0.05). These absolute values of the slope were significantly different ($p = 1.9\times10^{-5}$, N = 10). We reckoned that these two fronts of opposite directions might reveal distinct microtubule dynamics close and far from the chromosomes. Indeed, we expect the kMT to be numerous enough to be detected close to chromosomes but vastly overwhelmed by sMT at the location of the centrosome front (Redemann et al., 2017).

To safeguard against artefacts due to FRAP, we repeated the experiment using photoconversion (see Methods § Imaging condition for photobleaching and photoconversion experiments). We crossed strains with labellings of the microtubules mEOS3.2::TBB-2$^{\beta\text{-tubulin}}$ and the centrosomes mCherry::TBG-1$^{\gamma\text{-tubulin}}$. We used this second label to register the images over time, similarly to the FRAP experiment method. We produced the kymographs, and again, to cope with the low SNR, we averaged them across embryos after aligning them on the photoconverted region. We obtained a similar V-shaped pattern (Fig 1E) as expected. Indeed, the faint fluorescence signal at a high frame rate led to not viewing the region where photoconverted tubulin dimers are diluted with non-photoconverted ones. We concluded that the two fronts are not artefactual and may represent mechanisms related to microtubule dynamics.

To challenge the link between the observed fronts and microtubule dynamics, we set to decrease the growth rate of microtubules globally. ZYG-9$^{\text{XMAP215}}$ was a proper candidate as it affects all microtubules, astral, spindle and the ones attached at the kinetochores (Encalada et al., 2005; Fernandez et al., 2009; Lacroix et al., 2018; Srayko et al., 2005). However, we restricted ourselves to a partial depletion to preserve a functional spindle assembly (Matthews et al., 1998). We observed a late rotation of the spindle, confirming the penetrance of the treatment (Bellanger et al., 2007). We then performed the FRAP experiments and measured the absolute value of the slopes of the fronts (Fig 1G, S5I). We observed a significant decrease in the slopes on both the chromosome and the centrosome sides. It suggests that microtubule dynamics contribute to the mechanisms accounting for these fronts.

bioRxiv preprint doi: https://doi.org/10.1101/2022.11.07.515476; this version posted November 7, 2022. The copyright holder for this preprint (which was not certified by peer review) is the author/funder. All rights reserved. No reuse allowed without permission.

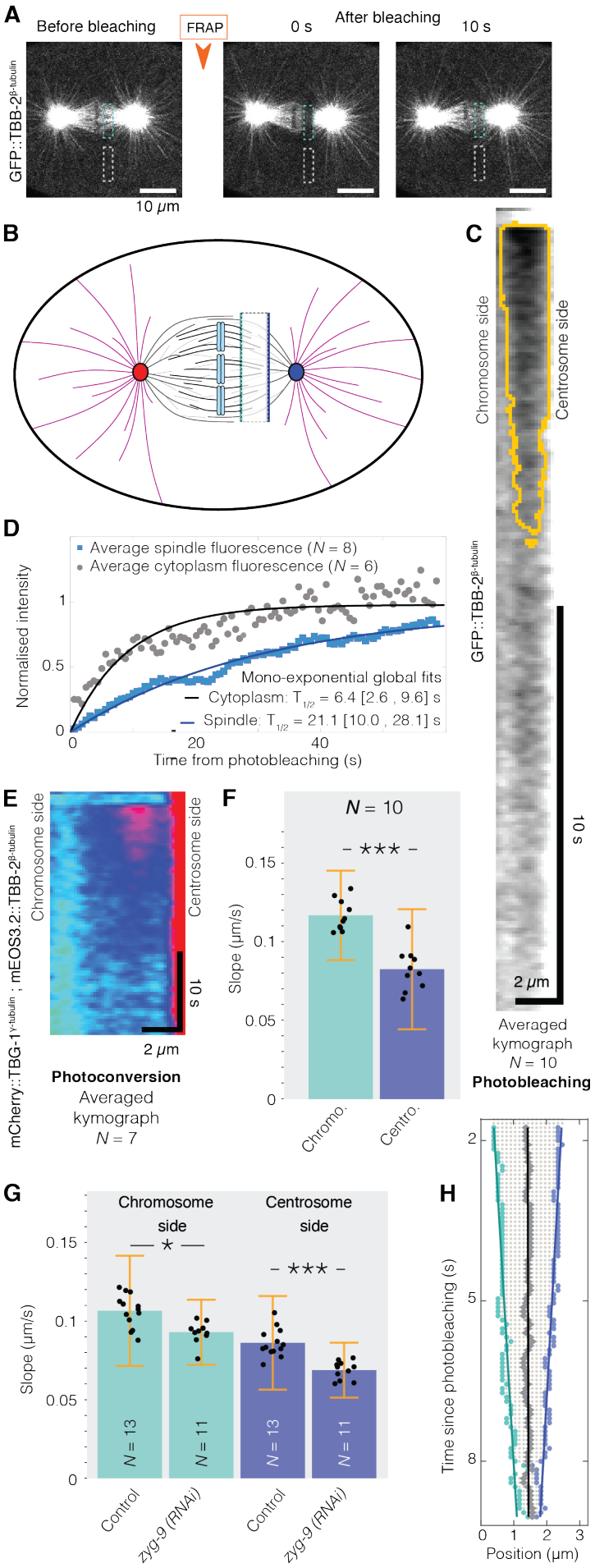

bioRxiv preprint doi: https://doi.org/10.1101/2022.11.07.515476; this version posted November 7, 2022. The copyright holder for this preprint (which was not certified by peer review) is the author/funder. All rights reserved. No reuse allowed without permission.

Figure 1: Tubulin fluorescence recovery after photobleaching and photoconversion in the metaphasic spindle of *C. elegans*. (**A**) Representative confocal live images before and after photobleaching (time above the stills). The posterior centrosome is on the right-hand side. Microtubules are labelled with GFP::TBB-2$^{\beta\text{-tubulin}}$. The scale bar corresponds to 10 µm. Blue and grey dashed boxes depict the regions used to assess fluorescence recovery in the spindle and cytoplasm, respectively. (**B**) Schematics of the FRAP experiment to measure front displacements. Thick dark grey lines depict the spindle microtubules emanating from (red) anterior and (blue) posterior centrosomes; thin light grey ones, the one branching from other microtubule lattices. Black lines correspond to kinetochore microtubules bound to (blue bars) the condensed sister chromatids. Astral microtubules are depicted in purple colour. The dashed box corresponds to the bleached area. The blue bars represent the measurement location of the fronts on (dark blue) the chromosome and (light blue) the kinetochore sides. (**C**) Averaged kymograph over the posterior half-spindle of $N = 10$ GFP::TBB-2$^{\beta\text{-tubulin}}$ labelled embryos. The centrosome was located on the right-hand side. The orange line delineates the bleached region as obtained by our analysis (Methods § Automatic recognition of the bleached region border). (**D**) Fluorescence recovery averaged over GFP::TBB-2$^{\beta\text{-tubulin}}$ non-treated embryos bleached: (blue) $N = 8$ in the spindle and (grey) $N = 6$ in the cytoplasm. Lines correspond to the global fit by a single exponential model (Giakoumakis et al., 2017) (see main text). The corresponding half-life is reported with the 95 % confidence interval within brackets. (**E**) Averaged kymograph after photoconversion within the mitotic spindle over $N = 7$ mEOS3.2::TBB-2$^{\beta\text{-tubulin}}$ with mCherry::TBG-1$^{\gamma\text{-tubulin}}$ embryos. The colour scale ranges from blue for dark pixels to red for bright areas. The centrosome was located on the right-hand side. (**FG**) Front velocities by segmenting the bleached region of (F) $N = 10$ GFP::TBB-2$^{\beta\text{-tubulin}}$ non-treated embryos; (G) $N = 11$ *zyg-9(RNAi)* treated embryos and $N = 13$ control ones. Black dots represent the average of N-1 embryos, leaving out, in turn, each embryo (Jackknife, Methods § Statistics on kymograph front slopes). Error bars are estimated standard errors using Jackknife resampling. Light blue bars are values on the chromosome side and dark blue on the centrosome side. (**H**) Linear fits of the edges of the segmented kymograph averaged over the non-treated embryos reported in panels C and F. Grey dots depict the pixels in the bleached region. Boundaries are highlighted by coloured dots on (turquoise, left edge) the chromosome side and (blue, right edge) the centrosome side. Grey diamonds depict the region mid-line. Linear fits are reported as lines of corresponding colours.

The dynamics of the centrosomal microtubules account for the corresponding recovery front.

The most obvious possibility to account for the observed fronts is a flux of the microtubules themselves. While a poleward flux of kMTs was not observed in the nematode, it is well-known in numerous other species. In contrast, an anti-poleward flux of sMT appeared much more unlikely. The edge of the bleached region on the centrosome side is located at about half the distance between the chromosomes and the spindle pole; at this place, the sMTs are three times more numerous than the kMTs. We wondered whether a fraction of the sMTs, large enough to be detected by FRAP, may move toward the chromosomes. We measured the displacement of the microtubule plus-ends within the spindle using EBP-2^{EB1} (Srayko et al., 2005). We imaged the doubly labelled strain EBP-2^{EB1}::mKate2; GFP::TBB-2$^{\beta\text{-tubulin}}$ at two frames per second to keep the SNR high. We registered these images over time to suppress the effect of spindle displacement as described above, then denoised the images with the Kalman filter (Kalman, 1960) (Fig S2A) and formed the kymograph as previously done (Fig S2B). We then measured the microtubule plus-ends velocity using the directionality ImageJ plugin within Fiji (Methods § Measuring the growth rate of microtubule plus ends), disregarding whether this velocity is due to microtubule growth or displacement (Liu, 1991; Schindelin et al., 2012; Schneider et al., 2012). We obtained a histogram of EBP-2^{EB1} comet speed (Fig S2C). We noticed that the distribution of comet orientation angles for a single embryo corresponded to a single Gaussian (S2D). We thus performed a global fit of individual embryos transforming angles into velocities (equation in Methods § Measuring the growth rate of microtubule plus ends) and found a growth rate of 0.98 ± 0.02 µm/s (average and standard deviation of the Gaussian), consistent with previous measurements (Lacroix et al., 2018; Srayko et al., 2005). It suggested that a single dynamical behaviour is present far from the chromosomes, likely corresponding to the growing microtubules.

We reckoned that the front displacement on the centrosome side might be accounted for by the dynamics of the sMTs (growth and shrinkage) combined with diffraction due to imaging. Indeed, the fast recovery after photobleaching within the cytoplasm suggested that non-bleached tubulin is available within seconds to enable the microtubules to grow with bright dimers in the bleached

bioRxiv preprint doi: https://doi.org/10.1101/2022.11.07.515476; this version posted November 7, 2022. The copyright holder for this preprint (which was not certified by peer review) is the author/funder. All rights reserved. No reuse allowed without permission.

area. We modelled this effect through the sMT dynamics after (Zelinski et al., 2012), assuming that the fluorescence intensity is a *bona fide* readout of microtubule density (Methods § Modelling the kymograph after photobleaching the spindle). We used microtubule dynamics parameters from previous measurements in nematode zygote (Table 3) (Kozlowski et al., 2007; Lacroix et al., 2018; Srayko et al., 2005). We considered chromatids as impassable obstacles (Schneider et al., 2021), leading to an increased catastrophe rate at this obstacle. Recovery after photobleaching for the sMTs was accounted for by the dynamic instability of the microtubules. In the model, it came to scaling over time the distribution of the sMTs in the bleached region (Fig S3A). In the light of bulk recovery (Fig 1D) and a previous publication (Redemann et al., 2017), the recovery scaling factor was modelled as a single exponential, with the half-life measured above.

We superimposed a second population of microtubules, corresponding to the kMTs, whose minus ends are uniformly distributed along the half-spindle (Redemann et al., 2017) (Fig S3E). In our simulation, these microtubules were assumed to flux towards the pole at 0.1 μm/s corresponding to the measured value. It is, however, noteworthy that modelling on the chromosome side remains heuristic. We formed a pseudo kymograph and observed a homogenous recovery of the whole bleached region (Fig S3D) superimposed to a front moving on the chromosome side.

We reckoned that the analysed images are affected by diffraction – a well-known phenomenon in optical microscopy imaging recapitulated by convolving images with a point spread function (PSF). We modelled it by a Gaussian PSF, whose standard deviation was obtained by fitting the experimentally measured PSF and read 149 nm (Methods § Diffraction due to microscope imaging) (Kirshner et al., 2013). We convolved the spatial dimension of our kymograph with this PSF and could then simulate a kymograph mimicking the experimental one (Fig 2A compared to Fig S3D). In other words, the combination of recovery due to microtubule dynamic instability and diffraction caused by imaging created a front on the centrosome side (compare Fig 2A and S3D). We then segmented the simulated bleached area and measured the front velocity using the same method as in the experimental case (Methods § Kymograph segmentation *et seq.*). We obtained 0.12 μm/s on the centrosome side, consistently with experiments. Overall, the bare growth and shrinking of the microtubules emanating from the centrosome restored fluorescence within the bleached area (Fig S3A). Combined with the diffraction due to microscope imaging, it led to an apparent front moving. It could account for the recovery seen on the centrosome side even in the absence of flux of these microtubules and without kinetochore microtubules (Fig S3B). In this latter case, the front motions, without flux, were predicted to be almost identical on both sides. Adding fluxing kinetochore microtubules broke this symmetry in agreement with experiments (Fig S3C).

We set out to challenge the proposed model experimentally. In the *zyg-9(RNAi)* experiment above, we observed a decrease in the slope, which is consistent with model predictions considering that ZYG-9^{XMAP215} increases the microtubule growth rate and the nucleation rate (Bellanger and Gönczy, 2003; Brouhard et al., 2008; Srayko et al., 2005; Srayko et al., 2003). We transcribed this latter in our model as promoting rescue or preventing catastrophe. In a broader take, we predicted that the slope on the centrosome side scaled inversely with the length of the spindle (Fig 2C). We tested the correlation between the spindle length and the front velocity on the centrosome side in all experiments presented in this article (Fig 2B). We observed a clear anti-correlation (Pearson $r = -0.66$, $p = 0.001$) as predicted by the model (Fig 2C). It was indicative of a global regulation since such an anti-correlation was seen across variegated depletions, including the microtubule dynamics either overall (ZYG-9, e.g.), either at the centrosome (KLP-7) or kinetochore (NDC-80, CLS-2). We thus tested the effect of the cell size, depleting ANI-2 and C27D9.1, but the limited variations did not allow us to be conclusive (Supplemental text). Since microtubule dynamics caused the font on the centrosome side, finding it dependent on spindle length is consistent (Fu et al., 2015; Maffini et al., 2009; Nehlig et al., 2020). Interestingly, such an anti-correlation was not seen experimentally on the slope on the chromosome side (Fig S4). It is consistent with the model prediction (Fig 2C). We concluded that the front motion closing the bleached area on the centrosome side was likely

bioRxiv preprint doi: https://doi.org/10.1101/2022.11.07.515476; this version posted November 7, 2022. The copyright holder for this preprint (which was not certified by peer review) is the author/funder. All rights reserved. No reuse allowed without permission.

not caused by any microtubule flux. It was instead caused by the combination of spindle microtubule dynamics and microscopy imaging.

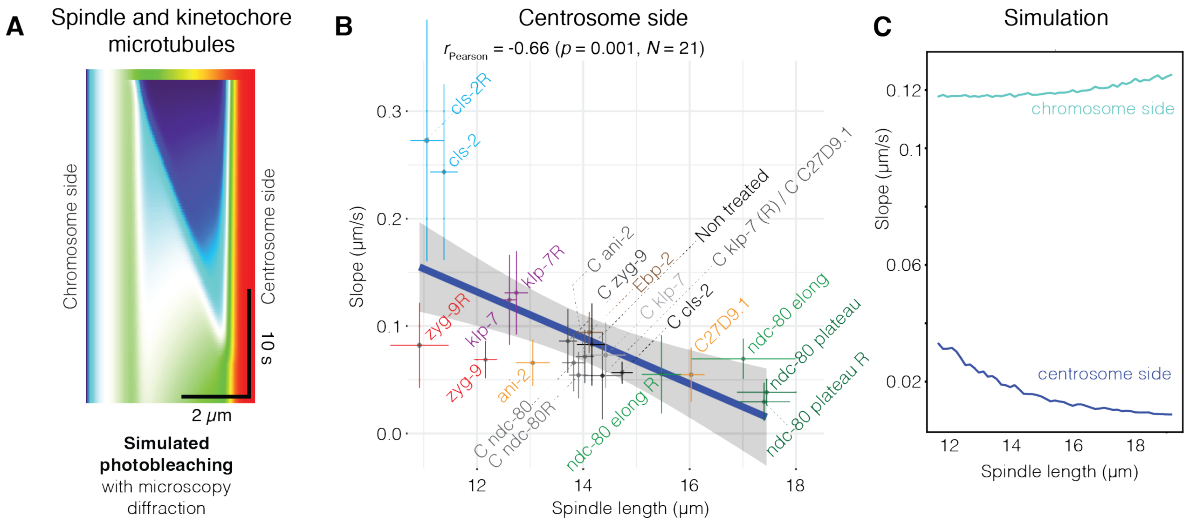

Figure 2: Front velocity on the centrosome side did not require flux but depended on spindle length. (**A**) Simulated kymograph including not-fluxing sMTs and kMTs submitted to poleward flux. It also mimicked diffraction by microscopy imaging (Methods § Modelling the kymograph after photobleaching the spindle). Corresponding simulated slopes read 0.12 µm/s on the chromosome side and 0.016 µm/s on the centrosome side. The colour scale ranges from blue for dark pixels to red for bright areas. Simulation parameters are reported in table 3. (**B**) The front velocities on the centrosome side anti-correlate with the spindle lengths. The formers were measured in various conditions (indicated) by segmenting the bleached region. We used strains with labelled microtubules GFP::TBB-2$^{\beta\text{-tubulin}}$. Spindle length was measured at the time of bleaching. The conditions are detailed in other figures. Suffix R stands for replica experiment and C for the control experiment attached to the mentioned treatment. Pearson correlation coefficient and the corresponding test are indicated above the plot. Error bars are standard errors. (**C**) The model predicted an anti-correlation between (turquoise) the centrosome-side front slope and the spindle length. (black) In contrast, no correlation was predicted on the chromosome side, matching the experimental observation (Fig S4).

A poleward flux of kinetochore microtubules may account for the chromosome-side recovery.

Because we have not seen a correlation between the spindle length and the recovery front velocity on the chromosome side, in contrast to the centrosome side, we reckoned that a second mechanism might superimpose specifically on the chromosome side. Indeed, the mechanism combining microtubule dynamics and microscopy-caused diffraction is expected to act on both edges of the bleached region. The most obvious addition would involve the kinetochore-microtubules growing at their plus ends, i.e. at the chromosomes, while sliding towards the poles and thus along the spindle microtubules. Consistently, depletion of ZYG-9$^{\text{XMAP215}}$, which decreases the polymerisation rate at the plus ends, reduced the front velocity on the chromosome side (Fig 1G). This hypothesis is consistent with Redemann and colleagues not measuring this poleward flux. Indeed, the kMTs are abundant compared to the sMTs only close to the chromosomes (Redemann et al., 2017). To challenge this hypothesis, we targeted the attachment of microtubules to the kinetochore by partially depleting a key player, NDC-80, in such a condition that chromosome segregation eventually succeeded in anaphase. We observed that the spindle in metaphase elongates during early metaphase (further termed early elongation) and plateaus before the anaphase onset, as previously reported (Fig S5A) (Cheerambathur et al., 2013). We studied the microtubule dynamics by FRAP during both phases (Fig 3AB). During the early elongation, the front velocity on the chromosome side increased, while during the plateau, it decreased compared to the control. Such

bioRxiv preprint doi: https://doi.org/10.1101/2022.11.07.515476; this version posted November 7, 2022. The copyright holder for this preprint (which was not certified by peer review) is the author/funder. All rights reserved. No reuse allowed without permission.

a result suggested that the kinetochore-microtubule attachment was involved in settings the corresponding front velocity. Because the measured effects were mild, we repeated the experiment and obtained similar results (Fig S5C). Our partial depletion of NDC-80 led to a delay in microtubule attaching end-on to the kinetochores (Cheerambathur et al., 2013; Cheeseman et al., 2004; Lange et al., 2019). Thus, kinetochore-microtubule attachments could not bear a normal load during the early elongation. It might account for the increased front velocity if the kMTs underwent a poleward flux. Later, during the plateau, we observed a velocity similar to or slightly reduced compared to the control. Because our conditions are hypomorphic, we attributed this phenotype to chromosome attachments that ended up being end-on, combined with a slower polymerisation rate at the kMT plus ends (Cheerambathur et al., 2017). This observation is suggestive that growing kMTs at the kinetochores may be necessary for the mechanism causing the observed chromosome recovery front.

We next wondered about the high recovery-front velocity observed on the chromosome side during the early elongation in *ndc-80(RNAi)*-treated embryos. We reckoned that a lack of NDC-80 leads to chromosome attachment being poorly able to bear the load related to kMT poleward motion (Cheerambathur et al., 2017; Suzuki et al., 2016). Therefore, we suspected that this increased velocity is the combination of a fraction of the kMTs having the expected behaviour and some detaching from the kinetochores under the tension and quickly sliding towards the spindle pole. If so, we expect a decreased density of microtubules close to the chromosomes, where kMTs are in the majority at the time of early elongation. We analysed the images by keeping the registration along time and extracted the fluorescence of a 6.5 µm height profile along the spindle axis, averaged over 1 s. We normalised the fluorescence and the position along the spindle before averaging profiles across embryos (Methods § Quantification of spindle fluorescence). We focused on the non-bleached anterior spindle half and observed a decrease during the early elongation compared to the control (Fig 3C). We concluded that some kMTs are likely pulled out from kinetochores at the time of early elongation accounting for the high recovery front on the chromosome side. It is also consistent with the spindle breaking with poles moving apart without separating chromosomes upon a stronger depletion of NDC-80 (Cheerambathur et al., 2017).

In the classic poleward-flux mechanism, CLS-2^{CLASP} is critical to ensure that the microtubules switch to polymerisation while undergoing flux (Arpag et al., 2020; Cheeseman et al., 2005). We thus partially depleted this protein. We observed a shorter spindle during metaphase, as expected (Cheeseman et al., 2005) (Fig S5B). We monitored the front velocity using our FRAP assay and found an increased velocity on the chromosome side that recalled the one observed during the precocious spindle elongation upon *ndc-80(RNAi)* (Fig 3DE, S5D). We interpreted it similarly: kMT were pulled out from the kinetochores causing the increased front velocity. Indeed, CLS-2 is also needed to allow the end-on attachment of the kMTs to bear the load (Cheeseman et al., 2005). Consistently, upon strong depletion, the spindle breaks due to the cortical pulling forces (Cheerambathur et al., 2017; Cheeseman et al., 2005). Our experiment suggests that the observed recovery front on the chromosome side, attributed to kinetochore-microtubule fluxing towards the poles, requires microtubule polymerisation.

bioRxiv preprint doi: https://doi.org/10.1101/2022.11.07.515476; this version posted November 7, 2022. The copyright holder for this preprint (which was not certified by peer review) is the author/funder. All rights reserved. No reuse allowed without permission.

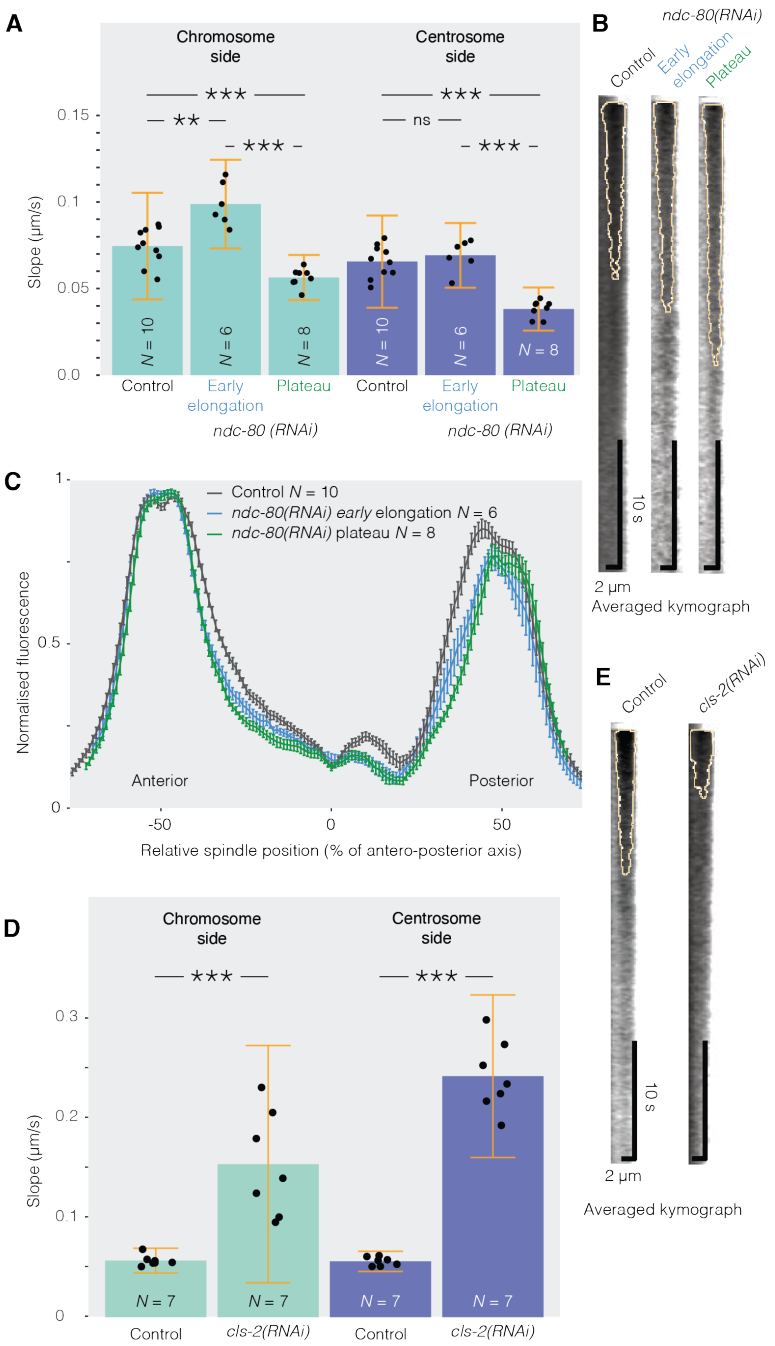

Figure 3: Front velocity on the chromosome side requires kMT polymerizing at the plus-ends. (**A**) Front velocities by segmenting the dark region of $N = 6$ *ndc-80(RNAi)* embryos bleached during early elongation, $N = 8$ *ndc-80(RNAi)* bleached during spindle length plateau and their $N = 10$ controls (Fig S5A). Microtubules were labelled using GFP::TBB-2$^{\beta\text{-tubulin}}$. Black dots represent averages of N-1 embryos, leaving out, in turn, each embryo (Jackknife, Methods § Statistics on kymograph front slopes). Error bars are estimated standard errors using Jackknife resampling. Light blue bars are values on the chromosome side and dark blue on the centrosome side. The experiment was replicated (Fig S5C). (**B**) Averaged kymograph over the posterior half-spindle for the data presented in (A), with centrosome on the right-hand side. The orange line delineates the bleached region as obtained by our analysis (Methods § Automatic recognition of the bleached region border). (**C**) Fluorescence intensity profile of $N = 6$ *ndc-80(RNAi)* bleached during early elongation, $N = 8$ *ndc-80(RNAi)* bleached during spindle length plateau and their $N = 10$ controls, labelled using GFP::TBB-2$^{\beta\text{-tubulin}}$ (Methods § Quantification of spindle fluorescence). They correspond to embryos analysed in panel A and Fig S5C combined. (**D**) Front velocities after segmenting the bleached region of $N = 7$ *cls-2(RNAi)* embryos and their $N = 7$ controls measured and represented in the same fashion as in A. The experiment was replicated (Fig S5D). (**E**) Averaged kymograph of the mitotic spindle for the data reported in (D), represented similarly to (B).

bioRxiv preprint doi: https://doi.org/10.1101/2022.11.07.515476; this version posted November 7, 2022. The copyright holder for this preprint (which was not certified by peer review) is the author/funder. All rights reserved. No reuse allowed without permission.

EBP-2[EB1] is a member of a minimal treadmilling system (Arpag et al., 2020). We thus performed a similar FRAP experiment and analysis under null mutant condition *ebp-2(*gk756*)* (Fig S6). We found a mild reduction of the recovery-front rate on the chromosome side, consistent with the lack of strong phenotype previously reported (Kamath et al., 2003; Sonnichsen et al., 2005). However, several proteins involved in the kinetochore may be impacted by EBP-2 depletion, like SKA-1 (Lange et al., 2019) or dynactin subunit DNC-2[p-50] (Barbosa et al., 2017). Overall, we concluded that the recovery front on the chromosome side is due to a mechanism dependent on kinetochore-microtubule attachment and polymerisation. It is thus distinct from the cause of the centrosome-side front. It also suggests that kinetochore microtubules may move locally poleward in a mechanism reminiscent of the poleward flux, despite being too short to reach the centrosome.

The poleward flux of kinetochore microtubules is spatially restricted.

In other organisms, the poleward flux involves all the microtubules, although their dynamics may differ (Conway et al., 2022; Risteski et al., 2022; Zhai et al., 1995). Dalton and co-authors proposed that the spindle undergoes gelation to account for the solid poleward motion of the microtubules within spindles prepared from *Xenopus laevis* extracts (Dalton et al., 2022). In contrast, we propose that only the kMTs undergo a poleward flux. As their number decreases with distance from the kinetochore (Redemann et al., 2017), the flux can be seen as restricted close to the kinetochores. To challenge this idea, we performed FRAP experiments bleaching a smaller area located either close or far from the spindle pole (Fig 4A). The low SNR combined with the narrower bleached region make the slope measurements more dispersed. We obtained similar front velocities, both moving inwards, on the chromosome and centrosome sides, when far from the kinetochores. It suggested that in this region of the spindle, both fronts reflected similar mechanisms (Fig 4B). Because the sMTs are in the vast majority compared to the kMTs in this spindle region, we suggest that recovery was only due to the microtubule dynamics combined with imaging diffraction, as detailed above. Close to the kinetochore, we measured higher front velocities on the chromosome side consistent with our previous measurement (Fig 1F). This experiment supports our hypothesis that only the kMTs are undergoing poleward flux. It also accounts for the difference between our findings and previous measurements because the kMT flux could only be seen close to the chromosomes (Labbe et al., 2004; Redemann et al., 2017). Anywhere else, the non-fluxing sMTs, which are in the majority, hide the kMTs.

Electronic micrographs reported that about a quarter of the kMTs reaches the corresponding pole (Redemann et al., 2017). Besides, half of the microtubules has opened minus-ends at the centrosomes (O'Toole et al., 2003). We wondered whether these could account for the flux observed. If long microtubules are essential contributors to the poleward flux, we expected them to depolymerise at their minus ends. In its minimal instance, such treadmilling motion requires MCAK (Arpag et al., 2020). In C. *elegans*, this protein homolog, KLP-7, is also localised at the kinetochores and spindle poles (Han et al., 2015; Sarov et al., 2012). We depleted it and measured the front velocity again (Fig 4CD, S5E). We did not observe a decreased front velocity on the chromosomes side. It suggests that the kMTs reaching the centrosomes play a minor role, if any, in the observed front displacement. The trend was instead an increase in velocity that we attributed to a role of KLP-7 at the kinetochore, putatively facilitating the turnover of the kMTs (Jaqaman et al., 2010; Kline-Smith et al., 2004; Wordeman et al., 2007). We suggest that the kMT poleward flux is not restricted to the ones reaching the centrosomes. Overall, we conclude that the kMTs are undergoing a poleward flux, sliding along the sMTs, which are not moving in contrast.

bioRxiv preprint doi: https://doi.org/10.1101/2022.11.07.515476; this version posted November 7, 2022. The copyright holder for this preprint (which was not certified by peer review) is the author/funder. All rights reserved. No reuse allowed without permission.

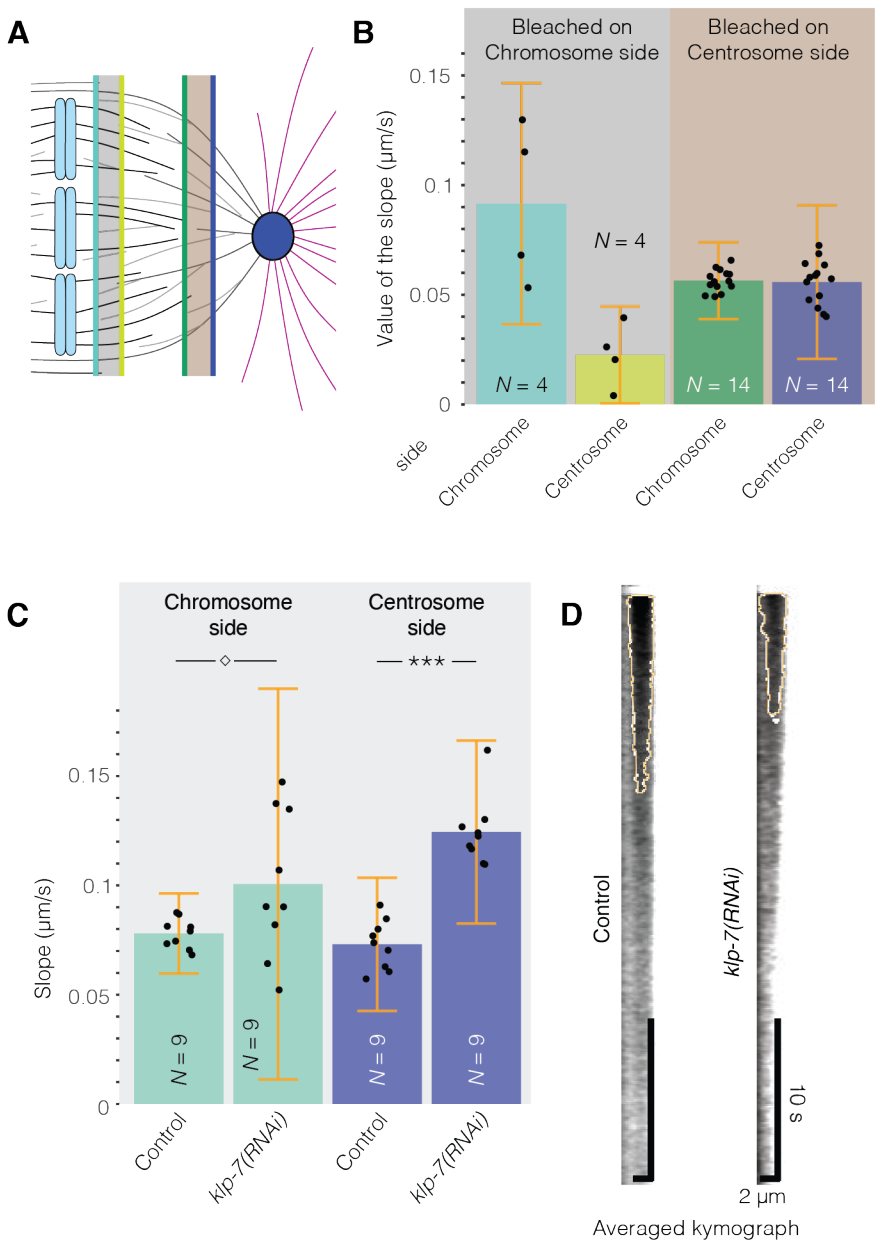

Figure 4: (**A**) Schematics of the FRAP experiment localized either close to chromosomes or centrosome to measure front displacement during recovery. Grey lines depict the spindle microtubules emanating from (blue) the posterior centrosome. Black lines correspond to the kinetochore microtubules bound to (blue bars) the condensed sister chromatids. The grey and maroon boxes are the bleached areas close to chromosomes and centrosome, respectively. The coloured lines depict the approximate positions of the front measurements corresponding to B. (**B**) Front velocities by segmenting the dark regions of $N = 10$ non-treated embryos, bleached either (grey background) close to chromosomes or (maroon background) close to centrosomes. Microtubules were labelled using GFP::TBB-2$^{\beta\text{-tubulin}}$. Black dots represent averages of N-1 embryos, leaving out, in turn, each embryo (Jackknife, Methods § Statistics on kymograph front slopes). Error bars are estimated using Jackknife resampling. The colour of the bars corresponds to the schematics (A). (**C**) Similar front-velocity analysis as in (B) for $N = 9$ *klp-7(RNAi)* treated embryos and $N = 9$ control ones. (**D**) Averaged kymograph over the posterior half-spindle for the data presented in (C), with centrosome on the right-hand side. The orange line delineates the bleached region as obtained by our analysis (Methods § Automatic recognition of the bleached region border).

bioRxiv preprint doi: https://doi.org/10.1101/2022.11.07.515476; this version posted November 7, 2022. The copyright holder for this preprint (which was not certified by peer review) is the author/funder. All rights reserved. No reuse allowed without permission.

DISCUSSION

We investigated the dynamics of the microtubules within the metaphasic spindle in the nematode one-cell embryo. While we confirmed the lack of global poleward flux by FRAP and photoconversion experiments, we showed that diffusion of tubulin dimers from the cytoplasm could not account for the recovery. We instead observed two opposed fronts closing the bleached region. From imaging microtubule plus-ends, we confirmed the fast growth of the spindle microtubules. Modelling such behaviour showed that it caused a uniform recovery of the bleached region. Such a dynamic-instability-caused uniform recovery combined with the diffraction by microscopy imaging is enough to account for the front motion on the centrosome side. Consistently, this front-recovery velocity anti-correlates with the spindle length in the various conditions tested in this paper.

In contrast, the front on the chromosome side appears to reflect a distinct mechanism superimposed on the mechanism at work on the centrosome side. While far from the chromosomes, one only sees the microtubule-dynamics-based recovery, and both velocities are similar, close to the chromosomes, the velocities differ between sides. We suggest that a subpopulation, namely the microtubules attached to the kinetochores, undergo poleward flux. They are in the majority over the other spindle microtubules only when looking close to kinetochores, making this additional mechanism visible only there. It accounts for the lack of detection of this flux in previous works (Labbe et al., 2004; Redemann et al., 2017). Two ranges of experiments support our hypothesis of the kMT flux: (i) A growth of the microtubules, while attached to the kinetochores, is needed to observe the chromosome side recovery, as found by partially depleting CLS-2^{CLASP} or ZYG-9^{XMAP215}. (ii) This flux is spatially restricted as depolymerisation at the centrosome, a task usually devoted to KLP-7^{MCAK}, is dispensable . Overall, we concluded that the kMTs are sliding towards the minus ends along the sMTs that remain static. It is noteworthy that we also found accelerated flux upon *ndc-80(RNAi)* and *cls-2(RNAi),* where the tension exerted by the microtubules on the kinetochore is low, as expected for poleward flux in other organisms (Matos et al., 2009). In light of the flux measurement close to the chromosomes, our suggested sliding mechanism contrasts with the previous proposal by Redemann and colleagues. Indeed, we found no indication that the kMTs are detaching from the centrosomes and moving towards the kinetochore. However, we cannot exclude that the kinetochore-microtubules depolymerise from their minus-end consistent with 38% of the ends opened in metaphase (Redemann et al., 2017).

Which mechanism could account for this sliding? Among the ones to be considered are the classic poleward flux drivers: (i) the depolymerisation at the minus end. This mechanism usually involves MCAK as the main microtubule depolymeriser (Arpag et al., 2020; Brust-Mascher et al., 2004). In our case, because the depletion of the homolog of MCAK, KLP-7, did not decrease the recovery velocity, rather tending to increase it, we consider this mechanism unlikely. We cannot exclude that other microtubule depolymerisers, like KLP-13, katanin, stathmin, and fidgetin, may contribute (Zhang et al., 2007). However, the depletion of KLP-13 has a reduced phenotype in the zygote (Kamath et al., 2003; Sonnichsen et al., 2005). Katanin was reported inactive during mitosis (Clandinin and Mains, 1993). Stathmin and fidgetin display a weak phenotype upon depletion in the one-cell embryo, making their implication unlikely (Kamath et al., 2003; Lacroix et al., 2014; Lacroix et al., 2016; Sonnichsen et al., 2005). (ii) The second possibility involves a molecular motor able to slide the kMTs along the sMTs as these latter are not undergoing poleward flux. We can therefore exclude mechanisms involving bridging microtubules (Jagric et al., 2021) or sliding of the overlapping (Miyamoto et al., 2004; Steblyanko et al., 2020; Uteng et al., 2008). Natural candidates are the kinesins BMK-1^{Eg5} and KLP-18, a kinesin-12 motor. These motors are involved during meiosis to organise the spindle microtubules (Cavin-Meza et al., 2022). However, during mitosis, BMK-1^{Eg5} depletion is not reported as having a strong phenotype but a faster elongation at anaphase (Saunders et al., 2007; Steblyanko et al., 2020). The KLP-18 alternative looks more

bioRxiv preprint doi: https://doi.org/10.1101/2022.11.07.515476; this version posted November 7, 2022. The copyright holder for this preprint (which was not certified by peer review) is the author/funder. All rights reserved. No reuse allowed without permission.

promising. Its mammal counterpart, KIF15, was shown to slide parallel microtubules *in vitro* (Drechsler and McAinsh, 2016). Furthermore, KLP-18 is also essential to correctly align the microtubules in the acentrosomal meiotic spindle of the nematode (Cavin-Meza et al., 2022; Wolff et al., 2021). It involves the sliding of parallel microtubules of the spindle. Finally, a plausible alternative to KLP-18-powered microtubule sliding is the transport of kMT minus ends to the poles by dynein using LIN-5^{NuMA} as an adapter. Such a mechanism was demonstrated in mammal cells, and NuMA antibody staining and reporting with a fluorescent construct (GFP-NuMA) indicate its presence at the spindle (Elting et al., 2014). (iii) Although the chromosomes are holocentric, C *elegans* is equipped with a chromokinesin, KLP-19. This kinesin is essential for zygote mitosis, and its depletion leads to chromosome-congression defects at metaphase as well as chromatin bridges and segregation errors in later phases (Powers et al., 2004). It is reasonable to imagine that it could move the kMTs towards the poles as a reaction to pushing the chromosomes to congress them. Steblyanko and colleagues proposed such a mechanism in human cells (Steblyanko et al., 2020). In a broader take and whatever the set of mechanisms at work in the nematode, the sliding force generators can be multiple as the above mechanisms can superimpose to ensure robustness. Furthermore, the discussed sliding mechanisms need to be coupled with the polymerisation of the microtubules at the kinetochore, like in other organisms, to maintain chromosome attachment (Barisic et al., 2021).

We wondered whether restricting the poleward flux to the kMTs is a peculiarity of nematodes. Indeed, metaphase is very brief in the nematode embryo, which prevents observing the spindle in a steady state. Furthermore, careful observation of the pole-to-pole distance during the metaphase shows a slow but constant length increase. This situation contrasts with the *Xenopus laevis* spindle prepared from extracts and at steady-state, where a gelification transition was observed (Dalton et al., 2022). A plausible cause of this difference is the strong pulling forces exerted on the spindle poles by the cortical force generators (Grill et al., 2001; Grill et al., 2003; Labbe et al., 2004). Compared to other cells, these forces are very high and participate in spindle elongation. One can speculate that sliding kMTs along the sMTs may mechanically insulate the kinetochores from the poles. In early metaphase, when pulling is weak, the sliding mechanism could generate enough force to ensure a correct function of the spindle assembly checkpoint and subsequent correcting of chromosome misattachments. Oppositely, in late metaphase, the hard pulling could be tempered down by letting the kMTs slide along the sMTs, leading to slow spindle elongation. Indeed, while the spindle slowly elongates in the non-treated embryos at that stage, decreasing cortical forces by depleting GPR-½ reduces this phenotype (Cheeseman et al., 2005; Lewellyn et al., 2010). It may maintain a level of tension at the kinetochores compatible with the SAC and correction mechanism function. Another important difference is the centromere organisation. Nematode chromosomes are holocentric; therefore, the kMTs do not assemble into a K fibre. However, a recent electron microscopy study suggests that enough space exists between microtubules in HeLa cells to accommodate molecular motors, making possible a mechanism similar to the one reported here (Kiewisz et al., 2022). Finally, it was recently reported in human cells that the dynamics of microtubules along the spindle axis are not uniform, meanwhile, minus-ends of the kMTs would also move towards the poles in a poleward flux (Conway et al., 2022; Risteski et al., 2022). Similarly, in HeLa cells, half of the kMTs does not reach the corresponding centrosomes (Kiewisz et al., 2022). This observation also suggests that a mechanism similar to our proposed for the nematode may occur in mammalian cells.

bioRxiv preprint doi: https://doi.org/10.1101/2022.11.07.515476; this version posted November 7, 2022. The copyright holder for this preprint (which was not certified by peer review) is the author/funder. All rights reserved. No reuse allowed without permission.

MATERIAL AND METHODS

C. *elegans* strains

All *C. elegans* strains were maintained at 20°C and cultured using standard procedures (Brenner, 1974). *C. elegans* worms were grown on NGM plates seeded with OP50 *E. coli* strain. *C. elegans* worm strains and genotypes are listed in Table 1.

Strain	Genotype	Crossing	Origin and reference
AZ244	unc-119(ed3) III; ruIs57[pie-1::GFP::tbb-2 +unc-119(+)] V		CGC (Praitis et al., 2001)
EU3068	ebp-2(or1954[ebp-2::mKate2]) II; ruIs57[pie-1::GFP::tbb-2 +unc-119(+)] V		CGC (Sugioka et al., 2018)
JEP120	ruIs57[pie-1::GFP::tbb-2 +unc-119(+)] V; gpr-2(ok1179) III.	AZ244 X TH291	TH291 is a 10x backcross of RB1150 (C. elegans Deletion Mutant Consortium, 2012)
JEP92	unc-119(ed3) ? III; ddIs180[WRM062cF05 spd-2:: 2xTY1 GFP FRT 3xFlag;unc-119(+)] ; ltIs5 [pIC36; pie-1/GFP-TEV-STag::kbp-1; unc-119 (+)]	OD9 x TH231	OD9: CGC (Cheeseman et al., 2004) TH231: (Decker et al., 2011)
JEP97	unc-119(ed3) ? III; ltIs37 [pAA64; pie-1/mCHERRY::his-58; unc-119 (+)]IV;ddIs44[WRM0614cB02 GLCherry::tbg-1;unc-119(+)]	OD56 x TH169	OD56: CGC (McNally et al., 2006) TH169: (Woodruff et al., 2015)
JEP166	ddIs44[WRM0614cB02 GLCherry::tbg-1;unc-119(+)]; pJD734_pSW077_Mos1_Pmex-5_mEOS3.2-tbb2	JEP97 x JDU562	JDU562: (Dias Maia Henriques, 2018)
JEP172	ebp-2(gk756) II; ruIs57[pie-1::GFP::tbb-2 +unc-119(+)] V	AZ244 x VC1614	VC1614: CGC (C. elegans Deletion Mutant Consortium, 2012)

Table 1: Worm strains used in this article and their genotypes.

RNAi treatment

RNAi was performed by feeding as described previously (Kamath and Ahringer, 2003; Timmons and Fire, 1998). The control embryos for the RNAi experiments were fed with bacteria carrying the empty plasmid L4440. We targeted *ndc-80* by RNAi using the same sequence as in (Cheerambathur et al., 2017) after cloning it into a vector. All other clones come from the Ahringer-Source BioScience library (Kamath et al., 2003). RNAi target, clone ID or sequence used, and feeding conditions are listed in Table 2. We set the RNAi treatment duration so that we did not notice any phenotype suggesting impaired meiosis.

bioRxiv preprint doi: https://doi.org/10.1101/2022.11.07.515476; this version posted November 7, 2022. The copyright holder for this preprint (which was not certified by peer review) is the author/funder. All rights reserved. No reuse allowed without permission.

Target	RNAi clone ID (Ahringer-Source Bioscience) or sequence used	IPTG concentration (mM)	Feeding time (hours)	Incubation temperature (°C)
cls-2	III-4J10	4	48	20
klp-7	III-5B24	4	48	25
zyg-9	II-6M11	4	8	25
ndc-80	Oligo 1: 5' – GGGGACAAGTTTGTACAAAAAAGCAGGCTTGGATGACAAGTACATTCAGAGATTATACAAATGATC – 3' Oligo 2: 5' – GGGGACCACTTTGTACAAGAAAGCTGGGTGGTGGTTCAAGATTCATTTGAATATTAAGTCCACTG – 3'	4	96	20
ani-2	II-4P19	2	48	25
C27D9.1	II-4A13	4	48	25

Table 2: RNAi target, clone ID and treatment conditions used in this article.

Microscopy: acquisition conditions

Preparation of C. elegans samples for imaging

C. elegans hermaphrodite adults were dissected in M9 medium (50 mM Na2HPO4, 17 mM KH2PO4, 86 mM NaCl, 1 mM MgSO4) (Brenner, 1974). The released embryos were then deposited on an agarose pad (2% w/v agarose, 0.6% w/v NaCl, 4% w/v sucrose) between slide and coverslip or between two 24x60 cm coverslips. To confirm the absence of phototoxicity and photodamage, we checked for normal rates of subsequent divisions (Riddle, 1997; Tinevez et al., 2012).

Imaging condition for photobleaching and photoconversion experiments

Embryo imaging was performed on a scanning confocal microscope with deconvolution (LSM 880 airyscan, Zeiss) using an apochromatic 63x/NA1.4 oil objective. Acquisition parameters were controlled by Zen black software. Imaging at 18°C was performed using the CherryTemp temperature control system (CherryBiotech, Rennes, France). We used two conditions: (1) With the AZ244 and JEP120 strains expressing GFP::TBB-2$^{\beta\text{-tubulin}}$, we performed photobleaching using an argon laser at wavelength 488 nm and 70 µW power for 75 iterations (photobleaching time ~ 1.9 s). We imaged using the same laser but at a 2.30 µW power. (2) With the TH65 and JEP65 strains expressing YFP::TBA-2$^{\gamma\text{-tubulin}}$, we used the argon laser at wavelength 514 nm and 20 µW power for 75 iterations (photobleaching time ~ 1.9 s). We imaged using the same laser but at a power of 1.50 µW. In all cases, five images were taken before photobleaching to get the basal fluorescence of the embryo. The laser power was measured at the objective output just before each microscopy session. We set to bleach a 2.6 x 19.5 µm area within the mitotic spindles (the embryo was oriented horizontally) (Fig 1B). When accommodating two bleached regions per half-spindle (Fig 4AB), their width read 1.3 µm. Images were acquired at 12.5 Hz.

bioRxiv preprint doi: https://doi.org/10.1101/2022.11.07.515476; this version posted November 7, 2022. The copyright holder for this preprint (which was not certified by peer review) is the author/funder. All rights reserved. No reuse allowed without permission.

In the case of photoconversion experiments, we used the strain JEP166 expressing mCherry::TBG-1$^{\gamma\text{-tubulin}}$ and mEOS3.2::TBB-2$^{\beta\text{-tubulin}}$. The mEOS3.2::TBB-2$^{\beta\text{-tubulin}}$ labelling was obtained from the JDU562 strain, a kind gift from Julien Dumont's team. The mCherry::TBG-1$^{\gamma\text{-tubulin}}$ channel enables the registration of the images on the position of the centrosomes (see § Automatic recognition of the bleached region border). Five images were taken before photoconversion to have the basal fluorescence of the embryo. Photoconversion was performed using a 405 nm UV laser at 10 µW for 35 iterations (photoconversion time ~ 0.850 s). We photoconverted a 13 x 1.3 µm area within the mitotic spindle after vertically orienting the anteroposterior axis of the embryo. Images were acquired with a 561 nm laser at 9 µW power and 3 frames per second. In all experiments, the anaphase onset was taken as a time reference. Images were stored using OMERO software (Li et al., 2016).

Imaging condition for measuring the velocity of microtubule plus-ends

Embryo imaging was performed on a scanning confocal microscope with deconvolution (LSM 880 airyscan, Zeiss) using an apochromatic 63x/NA1.4 oil objective. Acquisition parameters were controlled by Zen black software. Imaging at 18°C was performed using the CherryTemp temperature control system (CherryBiotech, Rennes, France). We also used focus maintaining for this particular experiment to compensate for drift. We measured microtubule plus-end comets' velocity to assess the microtubule growth rate. We used the strain EU3068 expressing EBP-2$^{\text{EB1}}$::mKate2; GFP::TBB-2$^{\beta\text{-tubulin}}$ (Sugioka et al., 2018). Image acquisition was performed with a HeNe laser at wavelength 594 nm and 3.35 µW power. The laser power was measured at the objective output at the beginning of each microscopy session. Images were acquired at 2 Hz on a single plane.

Image analysis

Automatic recognition of the bleached region border and measuring the slopes of the fluorescence-recovery fronts

Assembling a homogenous set of embryos

Observing the kymograph (Fig S2) suggested that the recovery proceeds by two fronts coming from each side. We set to measure the velocity of these fronts. We first selected images obtained in similar bleaching conditions by measuring laser power at each session. Indeed, the laser intensity may vary. Furthermore, the spindle lies 10-15 µm deep in the sample, further introducing variability. Overall, we considered only the experiments where the FRAP efficacy reached at least 30%, assessed by comparing the fluorescence intensities before and after the FRAP event. We checked that we performed bleaching during metaphase, i.e. between -120 and -30 s before the anaphase onset. It ensured a full fluorescence recovery prior to anaphase onset. Finally, the distance between the metaphasic plate and the bleached region was measured to ensure that a bright corridor separates the bleached region from the hollow due to the chromosomes, ensuring a robust measure of the chromosomal front speed.

Obtaining a kymograph for each embryo

We performed a rigid registration of the raw images using the slightly modified version of the so-called plugin (publicly available v. 1.4) under icy (de Chaumont et al., 2012). This registration focused on the centrosome position on the side of the bleached half-spindle, preventing a contribution of spindle displacement or rotation (Fig S1, S8A). We then applied a median filter under Fiji to limit the noise (Schindelin et al., 2012). We computed the kymograph by considering a region of interest of a length of 23.4 µm and a width of 3.12 µm (Fig S8B). To do so, we used Fiji and performed a median projection along a direction transverse to the spindle axis (Fig S8C).

Averaging kymograph over several embryos

bioRxiv preprint doi: https://doi.org/10.1101/2022.11.07.515476; this version posted November 7, 2022. The copyright holder for this preprint (which was not certified by peer review) is the author/funder. All rights reserved. No reuse allowed without permission.

To ensure that each embryo contributes equally, we performed a histogram equalisation among the individual embryos' kymographs using the histogramMatcher class in sciJava (interfaced using beanshell) (Rueden et al., 2021). Finally, we registered the kymographs aligning on the centrosome-side edge of the bleached region at the first time after bleach, using a supervised home-designed Matlab plugin (Fig S8C, arrowhead). We then averaged the kymographs pixel-wise (Fig S8D). We then cropped the embryo-averaged kymograph to consider only the 40 first seconds and the bleached half-spindle.

Kymograph segmentation

We next segmented the bleached area in the kymograph. As a preprocessing, we convolved the kymograph with a 3x3 kernel reading 5 in the central element and 1 elsewhere (Gaussian blur). We then autonomously detected the non-bleached area being conservative and considering only the pixels evidently non-bleached. To do so, we set the background class as the 60% brightest pixels. We then performed grey morphology (to remove micro/dot regions due to noise). Practically, we used two iterations of opening with a 1 pixel (130 nm) circular structural element and two closing iterations with the same element (Fig S8E, black line). Similarly, we set the bleached area as the 25% darkest pixels and performed the grey morphology (Fig S8E, orange line). To decide about the pixels of intermediate grey level, we set to use neighbourhood information. We trained a machine learning algorithm, namely random forests featuring 100 trees (Breiman, 2001), using the above classes for training and all kymographs in a set acquired under the same condition and side of the embryo. We then applied the algorithm to classify the pixels within the kymograph (Fig S8E, red line) using Weka under Fiji (beanshell script) (Arganda-Carreras et al., 2017). Finally, we performed grey morphology closing (2 pixels circle), watershed and the same closing again. It enabled us to remove dotty regions that are artefactual while preserving the largest one corresponding to the bleached area. We then selected the largest segmented object. Indeed, because the recovery is never complete (Fig 1C) and the contrast is low, it could create a small artefactual region in the tail of the main one. Finally, we dilated the shape using a 1px circle twice, making the resulting-shape convex.

Kymograph boundary fitting

Having segmented the bleached area, we fitted a line along the boundaries (between 2 and 30 s) to get the mean front velocities. We also computed the mid-curve (average between the positions of the two edges at each time point) and fitted it with a line.

Statistics on kymograph front slopes

We used a resampling method to get the error bars of the front velocities since we cannot perform the computation on individual embryos because images are too noisy. We used the Jackknife method, which requires computing the slope over a set containing all embryos but one (Efron and Tibshirani, 1993; Quenouille, 1956). We thus obtained a standard error on the averaged value estimated considering all embryos and could perform t-tests against the null hypothesis that the slope is 0. To compare conditions, we used the Jackknife again (Arvesen, 1969; Schechtman and Wang, 2004).

Statistics representation

For the sake of simplicity, we depicted confidence levels using diamonds or stars (***, $P \leq 0.0005$; **, $P \leq 0.005$; *, $P \leq 0.05$; ◇ $P \leq 0.1$; n.s., $P > 0.1$). This latter means non-significant.

bioRxiv preprint doi: https://doi.org/10.1101/2022.11.07.515476; this version posted November 7, 2022. The copyright holder for this preprint (which was not certified by peer review) is the author/funder. All rights reserved. No reuse allowed without permission.

Measuring the growth rate of microtubule plus ends

We measured the microtubule's growth rate by looking at their plus-end displacement. First, we registered the images using the GFP::TBB-2$^{\beta\text{-tubulin}}$ channel to keep the posterior centrosome immobile in the image stack as described above (Methods § Averaging kymograph over several embryos) (Fig S2A). We then denoised the EBP-2^{EB1}::mKate2 channel using the Kalman filter (Kalman, 1960). The EBP-2^{EB1} labelled plus-end displacement appears as an oblique line on the kymograph (Fig S2B). This latter was obtained by considering a region of interest of a length of 4.68 µm and a width of 3.12 µm centred on the posterior half-spindle. We formed the kymograph as previously described. We measured the direction and slope of these lines using the slightly modified version of the directionality plugin on ImageJ ((Tinevez et al., 2017), https://imagej.net/plugins/directionality). It produced a histogram counting the lines per direction (Fig S2D). We modelled the orientation distribution by a Gaussian. $a_d.e^{-(x-\mu_d)^2/2\sigma_d^2}$ where x is the orientation, μ_d the average orientation, σ_d the standard deviation and a_d the normalisation factor. However, the focus maintaining caused variable frame rates. We thus computed the velocity corresponding to direction distribution for each embryo and performed a global fit over all embryos, sharing the parameters to safeguard embryo-to-embryo variability again (Beechem, 1992). Practically, we used the model $\hat{a}.\exp\left(-(\mathrm{atan}(v.\frac{\tau}{\rho})-\mathrm{atan}(\hat{\mu}.\frac{\tau}{\rho}))^2 \Big/ 2\mathrm{atan}(\hat{\sigma}.\frac{\tau}{\rho})^2\right)$ with $\hat{a}$ the fit-estimated normalisation factor, v the velocity, τ the cycle time at imaging (different for each embryo), ρ the pixel size (resolution), $\hat{\mu}$ the estimated velocity and $\hat{\sigma}$ the standard deviation (Fig S2C).

Modelling the kymograph after photobleaching the spindle

Spindle- and kinetochore-microtubule dynamics

To support a semi-quantitative interpretation of the FRAP experiments upon depleting the putative players, we set to model the kymograph combining known microtubule dynamics and simulating the diffraction due to the microscope. We considered two microtubule populations within the spindle: one emanating from the centrosome and one attached to the kinetochore. In doing so, our analysis ignored the long-lived microtubules. These microtubules could be the few kMTs directly connecting the centrosome to the kinetochores, but their proportion is low (Redemann et al., 2017). They could also correspond to overlapping sMT. However, these latter were mostly expected around the metaphasic plate as it was suggested that the microtubules could hardly perforate the chromosome domain (Redemann et al., 2017; Schneider et al., 2022). The region of interest used in extracting the experimental kymograph did not include many of these, particularly when close to the kinetochores. Therefore, in modelling, we focused on the first 30 s after photobleaching.

We modelled the spindle microtubules (sMT) as free-growing microtubules until reaching the chromosomes (Zelinski et al., 2012). It resulted in an exponential-like decay of the microtubule density from the centrosome to the kinetochores, consistent with electronic microscopy imaging (Redemann et al., 2017). Microtubule dynamics parameters were obtained from the literature or our measurements (see table 3). At the kinetochore or chromosomes, modelled as an impassable obstacle (Schneider et al., 2021), we set the catastrophe rate there to 1. Indeed, varying by one order of magnitude around this value suggested that the density profile of the microtubules was poorly dependent on this parameter. Furthermore, such a rate corresponded to a 1 s residency time before detaching and was similar to observation on astral microtubules at the cell cortex (Bouvrais et al., 2021). It was about 5 times more than at free microtubule ends. We adjusted the spindle length as the distance between the two fluorescent centrosomes on the images, considering the intensity

bioRxiv preprint doi: https://doi.org/10.1101/2022.11.07.515476; this version posted November 7, 2022. The copyright holder for this preprint (which was not certified by peer review) is the author/funder. All rights reserved. No reuse allowed without permission.

profile extracted from the averaged kymograph of non-treated embryos during the 0.5 s after photobleaching. Technically, we smoothened the profile using a cubic spline and set the position of the peaks as the zero-crossings of the derivative.

We next modelled the kinetochore microtubules. Their minus ends are uniformly distributed along the spindle (Redemann et al., 2017). We assumed that the microtubules were permanently growing at the kinetochore due to the tension, as reported in other organisms (Cheeseman et al., 2004; Suzuki et al., 2015). The corresponding speed was set close to our observation, 0.1 µm/s. We set the ratio of sMT to kMT to 1.5 at 1 µm from the kinetochore after the electron micrograph (Fig S3C). Finally, we formed a pseudo kymograph (Fig S3D).

Recovery after Photobleaching

We then modelled the fluorescence recovery after photobleaching. We assumed no exchange of tubulin along the lattice. Recovery for the sMTs was accounted for by the dynamic instability of the microtubules. Technically, we modelled the bleaching as an entire disappearance of fluorescence in the corresponding region. About recovery, based on the fast diffusion in the cytoplasm, we assumed that fluorescent tubulin dimers are readily available and modelled the growth of bleached microtubules with fluorescent subunits. It came to scaling the curve in the bleached region with a coefficient (Fig S3A). This coefficient increased from 0 at bleaching time to 1 when reaching the total recovery. We modelled it as a single exponential with a characteristic time equal to 30.4 s measured in this study as the dynamics experimentally observed in the spindle. Doing so, we assumed that the sole free diffusion is involved, i.e. we modelled only the spindle microtubules while neglecting the contribution of the kMT. Recovery on the kinetochore side was attributed to the dynamic instability mechanism superimposed on the kMTs poleward flux due to their growth against the kinetochore (Fig S3C). The edges of the simulated bleached region corresponded to the value manually set during processing (methods § Averaging kymograph over several embryos). To do so, we measured the position of this edge on the centrosome side in non-treated embryos.

Diffraction due to microscope imaging

Finally, we imaged fluorescent beads of diameters 0.175 µm (PS-Speck Microscope Point Source) on the same microscope. We fitted the experimental image with a Gaussian (Kirshner et al., 2013) to obtain the PSF. We then convolved such a Gaussian, in 1D, with the simulated density of the microtubules at each time (Fig S3BC) and obtained a convolved kymograph mimicking the experimental kymograph (Fig 2A compared to Fig 1C).

Segmentation of the pseudokymograph

We analysed this kymograph similarly to the experimental one to extract the slopes of the fronts (Methods § Kymograph boundaries fitting) but only using a threshold at 13% on the intensity histogram.

Quantity	Value	Reference
MT growth rate	0.65 μm/s	(Srayko et al., 2005)
MT shrinking rate	0.84 μm/s	(Kozlowski et al., 2007)
Catastrophe rate	0.28 /s	(Lacroix et al., 2018)
Rescue rate	0.44 /s	(Lacroix et al., 2018)
Catastrophe against Chromosome	1 /s	(Bouvrais et al., 2021)
Spindle length	14.5 μm	This study

bioRxiv preprint doi: https://doi.org/10.1101/2022.11.07.515476; this version posted November 7, 2022. The copyright holder for this preprint (which was not certified by peer review) is the author/funder. All rights reserved. No reuse allowed without permission.

kMT poleward displacement	0.1 μm/s	This study
sMT recovery characteristic time	30.4 s	This study
Bleached region boundary from the centrosome	3.18 μm	This study
Bleached region width	2.6 μm	This study
PSF standard deviation	149 nm	This study

Table 3: Values used in the simulation and associated references.

Quantification of spindle fluorescence

We considered the registered images of the embryos used for FRAP analysis (Methods § Averaging kymograph over several embryos). We extracted a fluorescence profile along the spindle axis, which encompassed an averaging along the direction transverse to the spindle using a box of a width of 6.5 µm centred on the spindle. We then performed a 1 s box-average to obtain the per embryo profile just after the photobleaching. Because the illumination might change, we normalised the fluorescence intensity between 0 and 1.

Since the spindle length may vary, we also normalised the position along the spindle by the spindle length with 0 at the metaphasic plate. We then aligned the profile on the position of the metaphasic plate and averaged over the embryos.

Acknowledgements

The strains TH291, TH231, and TH169 are kind gifts from Prof A. A. Hyman. Dr J. Dumont kindly offered JDU562. We thank Dr Gregoire Michaux for the feeding clone library and technical support. We also thank Drs. Gilliane Maton, Fabrice Mahé, Christophe Heligon, Rebecca Smith, Sebastien Huet, Gregoire Michaux, Anne Pacquelet, Xavier Pinson, Marc Tramier and Ms Ostiane d'Augustin, for discussions about the project. Some strains were provided by the Caenorhabditis Genetics Center (CGC), funded by the National Institutes of Health Office of Research Infrastructure Programs (P40 OD010440; University of Minnesota). We also acknowledge La Ligue contre le cancer (comites d'Ille-et-Vilaine et du Maine-et-Loire). Microscopy imaging was performed at the Microscopy Rennes Imaging Center, UMS 3480 CNRS/US 18 INSERM/University of Rennes 1. In particular, we acknowledge the funding of the Zeiss Airyscan confocal microscope by EU funding FEDER under reference CARE Phase 2.

Author contributions

Conceptualisation: JP, LLM; Data curation: NS, LC, JP; Formal analysis: NS, LC, JP; Funding acquisition: JP, LLM; Investigation: NS, LC, SP, JP; Methodology: NS, HB, LC, JP; Project administration: JP; Software: NS, JP; Supervision: LLM, JP, LC; Validation: HB, LC, JP; Visualisation: NS, JP; Writing NS, JP; Writing – review and editing: LC, NS, JP, LLM, HB.

Conflict of interest

The authors declare that they have no conflict of interest.

bioRxiv preprint doi: https://doi.org/10.1101/2022.11.07.515476; this version posted November 7, 2022. The copyright holder for this preprint (which was not certified by peer review) is the author/funder. All rights reserved. No reuse allowed without permission.

References

Akhmanova, A., and Steinmetz, M.O. (2015). Control of microtubule organization and dynamics: two ends in the limelight. Nat Rev Mol Cell Biol *16*, 711-726.

Al-Bassam, J., and Chang, F. (2011). Regulation of microtubule dynamics by TOG-domain proteins XMAP215/Dis1 and CLASP. Trends Cell Biol *21*, 604-614.

Arganda-Carreras, I., Kaynig, V., Rueden, C., Eliceiri, K.W., Schindelin, J., Cardona, A., and Sebastian Seung, H. (2017). Trainable Weka Segmentation: a machine learning tool for microscopy pixel classification. Bioinformatics *33*, 2424-2426.

Arpag, G., Lawrence, E.J., Farmer, V.J., Hall, S.L., and Zanic, M. (2020). Collective effects of XMAP215, EB1, CLASP2, and MCAK lead to robust microtubule treadmilling. Proc Natl Acad Sci U S A *117*, 12847-12855.

Arvesen, J.N. (1969). Jackknifing U-Statistics. The Annals of Mathematical Statistics *40*, 2076-2100.

Axelrod, D., Koppel, D.E., Schlessinger, J., Elson, E., and Webb, W.W. (1976). Mobility measurement by analysis of fluorescence photobleaching recovery kinetics. Biophys J *16*, 1055-1069.

Bakhoum, S.F., and Compton, D.A. (2012). Kinetochores and disease: keeping microtubule dynamics in check! Curr Opin Cell Biol *24*, 64-70.

Bakhoum, S.F., Thompson, S.L., Manning, A.L., and Compton, D.A. (2009). Genome stability is ensured by temporal control of kinetochore-microtubule dynamics. Nat Cell Biol *11*, 27-35.

Barbosa, D.J., Duro, J., Prevo, B., Cheerambathur, D.K., Carvalho, A.X., and Gassmann, R. (2017). Dynactin binding to tyrosinated microtubules promotes centrosome centration in C. elegans by enhancing dynein-mediated organelle transport. PLoS Genet *13*, e1006941.

Barisic, M., Rajendraprasad, G., and Steblyanko, Y. (2021). The metaphase spindle at steady state - Mechanism and functions of microtubule poleward flux. Seminars in cell & developmental biology.

Beechem, J.M. (1992). Global analysis of biochemical and biophysical data. Methods Enzymol *210*, 37-54.

Bellanger, J.-M., and Gönczy, P. (2003). TAC-1 and ZYG-9 Form a Complex that Promotes Microtubule Assembly in C. elegans Embryos. Curr Biol *13*, 1488-1498.

Bellanger, J.M., Carter, J.C., Phillips, J.B., Canard, C., Bowerman, B., and Gonczy, P. (2007). ZYG-9, TAC-1 and ZYG-8 together ensure correct microtubule function throughout the cell cycle of C. elegans embryos. J Cell Sci *120*, 2963-2973.

Bouvrais, H., Chesneau, L., Le Cunff, Y., Fairbrass, D., Soler, N., Pastezeur, S., Pecot, T., Kervrann, C., and Pecreaux, J. (2021). The coordination of spindle-positioning forces during the asymmetric division of the Caenorhabditis elegans zygote. EMBO reports *22*, e50770.

Bouvrais, H., Chesneau, L., Pastezeur, S., Fairbrass, D., Delattre, M., and Pecreaux, J. (2018). Microtubule Feedback and LET-99-Dependent Control of Pulling Forces Ensure Robust Spindle Position. Biophys J *115*, 2189-2205.

Breiman, L. (2001). Random Forests. Machine Learning *45*, 5-32.

Brenner, S. (1974). The genetics of Caenorhabditis elegans. Genetics *77*, 71-94.

bioRxiv preprint doi: https://doi.org/10.1101/2022.11.07.515476; this version posted November 7, 2022. The copyright holder for this preprint (which was not certified by peer review) is the author/funder. All rights reserved. No reuse allowed without permission.

Brouhard, G.J., Stear, J.H., Noetzel, T.L., Al-Bassam, J., Kinoshita, K., Harrison, S.C., Howard, J., and Hyman, A.A. (2008). XMAP215 is a processive microtubule polymerase. Cell *132*, 79-88.

Brust-Mascher, I., Civelekoglu-Scholey, G., Kwon, M., Mogilner, A., and Scholey, J.M. (2004). Model for anaphase B: role of three mitotic motors in a switch from poleward flux to spindle elongation. Proc Natl Acad Sci U S A *101*, 15938-15943.

Brust-Mascher, I., Sommi, P., Cheerambathur, D.K., and Scholey, J.M. (2009). Kinesin-5-dependent poleward flux and spindle length control in Drosophila embryo mitosis. Mol Biol Cell *20*, 1749-1762.

C. elegans Deletion Mutant Consortium (2012). Large-scale screening for targeted knockouts in the Caenorhabditis elegans genome. G3 *2*, 1415-1425.

Cavin-Meza, G., Kwan, M.M., and Wignall, S.M. (2022). Multiple motors cooperate to establish and maintain acentrosomal spindle bipolarity in C. elegans oocyte meiosis. eLife *11*.

Chaaban, S., Jariwala, S., Hsu, C.T., Redemann, S., Kollman, J.M., Muller-Reichert, T., Sept, D., Bui, K.H., and Brouhard, G.J. (2018). The Structure and Dynamics of C. elegans Tubulin Reveals the Mechanistic Basis of Microtubule Growth. Dev Cell *47*, 191-204 e198.

Cheerambathur, D.K., Gassmann, R., Cook, B., Oegema, K., and Desai, A. (2013). Crosstalk between microtubule attachment complexes ensures accurate chromosome segregation. Science *342*, 1239-1242.

Cheerambathur, D.K., Prevo, B., Hattersley, N., Lewellyn, L., Corbett, K.D., Oegema, K., and Desai, A. (2017). Dephosphorylation of the Ndc80 Tail Stabilizes Kinetochore-Microtubule Attachments via the Ska Complex. Dev Cell *41*, 424-437 e424.

Cheeseman, I.M. (2014). The kinetochore. Cold Spring Harb Perspect Biol *6*, a015826.

Cheeseman, I.M., MacLeod, I., Yates, J.R., 3rd, Oegema, K., and Desai, A. (2005). The CENP-F-like proteins HCP-1 and HCP-2 target CLASP to kinetochores to mediate chromosome segregation. Curr Biol *15*, 771-777.

Cheeseman, I.M., Niessen, S., Anderson, S., Hyndman, F., Yates, J.R., 3rd, Oegema, K., and Desai, A. (2004). A conserved protein network controls assembly of the outer kinetochore and its ability to sustain tension. Genes Dev *18*, 2255-2268.

Cimini, D., Wan, X., Hirel, C.B., and Salmon, E.D. (2006). Aurora kinase promotes turnover of kinetochore microtubules to reduce chromosome segregation errors. Curr Biol *16*, 1711-1718.

Clandinin, T.R., and Mains, P.E. (1993). Genetic studies of mei-1 gene activity during the transition from meiosis to mitosis in Caenorhabditis elegans. Genetics *134*, 199-210.

Conway, W., Kiewisz, R., Fabig, G., Kelleher, C.P., Wu, H.Y., Anjur-Dietrich, M., Muller-Reichert, T., and Needleman, D.J. (2022). Self-organization of kinetochore-fibers in human mitotic spindles. eLife *11*.

Dalton, B.A., Oriola, D., Decker, F., Jülicher, F., and Brugués, J. (2022). A gelation transition enables the self-organization of bipolar metaphase spindles. Nature Physics *18*, 323-331.

de Chaumont, F., Dallongeville, S., Chenouard, N., Herve, N., Pop, S., Provoost, T., Meas-Yedid, V., Pankajakshan, P., Lecomte, T., Le Montagner, Y.*, et al.* (2012). Icy: an open bioimage informatics platform for extended reproducible research. Nat Methods *9*, 690-696.

bioRxiv preprint doi: https://doi.org/10.1101/2022.11.07.515476; this version posted November 7, 2022. The copyright holder for this preprint (which was not certified by peer review) is the author/funder. All rights reserved. No reuse allowed without permission.

Decker, M., Jaensch, S., Pozniakovsky, A., Zinke, A., O'Connell, K.F., Zachariae, W., Myers, E., and Hyman, A.A. (2011). Limiting amounts of centrosome material set centrosome size in C. elegans embryos. Curr Biol *21*, 1259-1267.

Dias Maia Henriques, A.M. (2018). Study of the Mechanisms of Chromosome Segregation in the C. elegans Embryo.

Drechsler, H., and McAinsh, A.D. (2016). Kinesin-12 motors cooperate to suppress microtubule catastrophes and drive the formation of parallel microtubule bundles. Proc Natl Acad Sci U S A.

Efron, B., and Tibshirani, R.J. (1993). An introduction to the bootstrap (New York ; London: Chapman & Hall).

Elting, M.W., Hueschen, C.L., Udy, D.B., and Dumont, S. (2014). Force on spindle microtubule minus ends moves chromosomes. J Cell Biol *206*, 245-256.

Elting, M.W., Suresh, P., and Dumont, S. (2018). The Spindle: Integrating Architecture and Mechanics across Scales. Trends Cell Biol *28*, 896-910.

Encalada, S.E., Willis, J., Lyczak, R., and Bowerman, B. (2005). A spindle checkpoint functions during mitosis in the early Caenorhabditis elegans embryo. Mol Biol Cell *16*, 1056-1070.

Fernandez, N., Chang, Q., Buster, D.W., Sharp, D.J., and Ma, A. (2009). A model for the regulatory network controlling the dynamics of kinetochore microtubule plus-ends and poleward flux in metaphase. Proc Natl Acad Sci U S A *106*, 7846-7851.

Fu, J., Bian, M., Xin, G., Deng, Z., Luo, J., Guo, X., Chen, H., Wang, Y., Jiang, Q., and Zhang, C. (2015). TPX2 phosphorylation maintains metaphase spindle length by regulating microtubule flux. J Cell Biol *210*, 373-383.

Gaetz, J., and Kapoor, T.M. (2004). Dynein/dynactin regulate metaphase spindle length by targeting depolymerizing activities to spindle poles. J Cell Biol *166*, 465-471.

Ganem, N.J., Upton, K., and Compton, D.A. (2005). Efficient mitosis in human cells lacking poleward microtubule flux. Curr Biol *15*, 1827-1832.

Gerhold, A.R., Poupart, V., Labbe, J.C., and Maddox, P.S. (2018). Spindle assembly checkpoint strength is linked to cell fate in the Caenorhabditis elegans embryo. Mol Biol Cell *29*, 1435-1448.

Giakoumakis, N.N., Rapsomaniki, M.A., and Lygerou, Z. (2017). Analysis of Protein Kinetics Using Fluorescence Recovery After Photobleaching (FRAP). Methods Mol Biol *1563*, 243-267.

Girao, H., and Maiato, H. (2020). Measurement of Microtubule Half-Life and Poleward Flux in the Mitotic Spindle by Photoactivation of Fluorescent Tubulin. Methods Mol Biol *2101*, 235-246.

Grill, S.W., Gonczy, P., Stelzer, E.H., and Hyman, A.A. (2001). Polarity controls forces governing asymmetric spindle positioning in the Caenorhabditis elegans embryo. Nature *409*, 630-633.

Grill, S.W., Howard, J., Schaffer, E., Stelzer, E.H., and Hyman, A.A. (2003). The distribution of active force generators controls mitotic spindle position. Science *301*, 518-521.

bioRxiv preprint doi: https://doi.org/10.1101/2022.11.07.515476; this version posted November 7, 2022. The copyright holder for this preprint (which was not certified by peer review) is the author/funder. All rights reserved. No reuse allowed without permission.

Han, X., Adames, K., Sykes, E.M., and Srayko, M. (2015). The KLP-7 Residue S546 Is a Putative Aurora Kinase Site Required for Microtubule Regulation at the Centrosome in C. elegans. PLoS One *10*, e0132593.

Hotani, H., and Horio, T. (1988). Dynamics of microtubules visualized by darkfield microscopy: treadmilling and dynamic instability. Cell Motil Cytoskeleton *10*, 229-236.

Jagric, M., Risteski, P., Martincic, J., Milas, A., and Tolic, I.M. (2021). Optogenetic control of PRC1 reveals its role in chromosome alignment on the spindle by overlap length-dependent forces. eLife *10*.

Jaqaman, K., King, E.M., Amaro, A.C., Winter, J.R., Dorn, J.F., Elliott, H.L., McHedlishvili, N., McClelland, S.E., Porter, I.M., Posch, M.*, et al.* (2010). Kinetochore alignment within the metaphase plate is regulated by centromere stiffness and microtubule depolymerases. J Cell Biol *188*, 665-679.

Kalman, R.E. (1960). A new approach to linear filtering and prediction problems. J Basic Eng *82*, 35-45.

Kamath, R.S., and Ahringer, J. (2003). Genome-wide RNAi screening in Caenorhabditis elegans. Methods *30*, 313-321.

Kamath, R.S., Fraser, A.G., Dong, Y., Poulin, G., Durbin, R., Gotta, M., Kanapin, A., Le Bot, N., Moreno, S., Sohrmann, M.*, et al.* (2003). Systematic functional analysis of the Caenorhabditis elegans genome using RNAi. Nature *421*, 231-237.

Kiewisz, R., Fabig, G., Conway, W., Baum, D., Needleman, D., and Muller-Reichert, T. (2022). Three-dimensional structure of kinetochore-fibers in human mitotic spindles. eLife *11*.

Kirshner, H., Aguet, F., Sage, D., and Unser, M. (2013). 3-D PSF fitting for fluorescence microscopy: implementation and localization application. J Microsc *249*, 13-25.

Kline-Smith, S.L., Khodjakov, A., Hergert, P., and Walczak, C.E. (2004). Depletion of centromeric MCAK leads to chromosome congression and segregation defects due to improper kinetochore attachments. Mol Biol Cell *15*, 1146-1159.

Kozlowski, C., Srayko, M., and Nedelec, F. (2007). Cortical microtubule contacts position the spindle in C. elegans embryos. Cell *129*, 499-510.

Kuhn, J., and Dumont, S. (2019). Mammalian kinetochores count attached microtubules in a sensitive and switch-like manner. J Cell Biol.

Labbe, J.C., McCarthy, E.K., and Goldstein, B. (2004). The forces that position a mitotic spindle asymmetrically are tethered until after the time of spindle assembly. J Cell Biol *167*, 245-256.

Lacroix, B., Bourdages, K.G., Dorn, J.F., Ihara, S., Sherwood, D.R., Maddox, P.S., and Maddox, A.S. (2014). In situ imaging in C. elegans reveals developmental regulation of microtubule dynamics. Dev Cell *29*, 203-216.

Lacroix, B., Letort, G., Pitayu, L., Salle, J., Stefanutti, M., Maton, G., Ladouceur, A.M., Canman, J.C., Maddox, P.S., Maddox, A.S.*, et al.* (2018). Microtubule Dynamics Scale with Cell Size to Set Spindle Length and Assembly Timing. Dev Cell *45*, 496-511 e496.

Lacroix, B., Ryan, J., Dumont, J., Maddox, P.S., and Maddox, A.S. (2016). Identification of microtubule growth deceleration and its regulation by conserved and novel proteins. Mol Biol Cell.

bioRxiv preprint doi: https://doi.org/10.1101/2022.11.07.515476; this version posted November 7, 2022. The copyright holder for this preprint (which was not certified by peer review) is the author/funder. All rights reserved. No reuse allowed without permission.

Lampson, M.A., and Grishchuk, E.L. (2017). Mechanisms to Avoid and Correct Erroneous Kinetochore-Microtubule Attachments. Biology (Basel) *6*.

Lange, K.I., Suleman, A., and Srayko, M. (2019). Kinetochore Recruitment of the Spindle and Kinetochore-Associated (Ska) Complex Is Regulated by Centrosomal PP2A in Caenorhabditis elegans. Genetics *212*, 509-522.

Lantzsch, I., Yu, C.H., Chen, Y.Z., Zimyanin, V., Yazdkhasti, H., Lindow, N., Szentgyoergyi, E., Pani, A.M., Prohaska, S., Srayko, M.*, et al.* (2021). Microtubule reorganization during female meiosis in C. elegans. eLife *10*.

Lewellyn, L., Dumont, J., Desai, A., and Oegema, K. (2010). Analyzing the effects of delaying aster separation on furrow formation during cytokinesis in the Caenorhabditis elegans embryo. Mol Biol Cell *21*, 50-62.

Li, S., Besson, S., Blackburn, C., Carroll, M., Ferguson, R.K., Flynn, H., Gillen, K., Leigh, R., Lindner, D., Linkert, M.*, et al.* (2016). Metadata management for high content screening in OMERO. Methods *96*, 27-32.

Liu, Z.Q. (1991). Scale space approach to directional analysis of images. Appl Opt *30*, 1369-1373.

Maddox, P., Desai, A., Oegema, K., Mitchison, T.J., and Salmon, E.D. (2002). Poleward microtubule flux is a major component of spindle dynamics and anaphase a in mitotic Drosophila embryos. Curr Biol *12*, 1670-1674.

Maddox, P., Straight, A., Coughlin, P., Mitchison, T.J., and Salmon, E.D. (2003). Direct observation of microtubule dynamics at kinetochores in Xenopus extract spindles: implications for spindle mechanics. J Cell Biol *162*, 377-382.

Maddox, P.S., Oegema, K., Desai, A., and Cheeseman, I.M. (2004). "Holo"er than thou: chromosome segregation and kinetochore function in C. elegans. Chromosome Res *12*, 641-653.

Maffini, S., Maia, A.R., Manning, A.L., Maliga, Z., Pereira, A.L., Junqueira, M., Shevchenko, A., Hyman, A., Yates, J.R., 3rd, Galjart, N.*, et al.* (2009). Motor-independent targeting of CLASPs to kinetochores by CENP-E promotes microtubule turnover and poleward flux. In Curr Biol (England), pp. 1566-1572.

Magidson, V., O'Connell, C.B., Loncarek, J., Paul, R., Mogilner, A., and Khodjakov, A. (2011). The spatial arrangement of chromosomes during prometaphase facilitates spindle assembly. Cell *146*, 555-567.

Maiato, H., Khodjakov, A., and Rieder, C.L. (2005). Drosophila CLASP is required for the incorporation of microtubule subunits into fluxing kinetochore fibres. Nat Cell Biol *7*, 42-47.

Matos, I., Pereira, A.J., Lince-Faria, M., Cameron, L.A., Salmon, E.D., and Maiato, H. (2009). Synchronizing chromosome segregation by flux-dependent force equalization at kinetochores. J Cell Biol *186*, 11-26.

Matsuda, T., and Nagai, T. (2014). Quantitative measurement of intracellular protein dynamics using photobleaching or photoactivation of fluorescent proteins. Microscopy (Oxf) *63*, 403-408.

Matthews, L.R., Carter, P., Thierry-Mieg, D., and Kemphues, K. (1998). ZYG-9, a Caenorhabditis elegans protein required for microtubule organization and function, is a component of meiotic and mitotic spindle poles. J Cell Biol *141*, 1159-1168.

bioRxiv preprint doi: https://doi.org/10.1101/2022.11.07.515476; this version posted November 7, 2022. The copyright holder for this preprint (which was not certified by peer review) is the author/funder. All rights reserved. No reuse allowed without permission.

McNally, K., Audhya, A., Oegema, K., and McNally, F.J. (2006). Katanin controls mitotic and meiotic spindle length. J Cell Biol *175*, 881-891.

McVey, S.L., Cosby, J.K., and Nannas, N.J. (2021). Aurora B Tension Sensing Mechanisms in the Kinetochore Ensure Accurate Chromosome Segregation. Int J Mol Sci *22*.

Mitchison, T.J. (1989). Polewards microtubule flux in the mitotic spindle: evidence from photoactivation of fluorescence. J Cell Biol *109*, 637-652.

Mitchison, T.J., and Salmon, E.D. (1992). Poleward kinetochore fiber movement occurs during both metaphase and anaphase-A in newt lung cell mitosis. J Cell Biol *119*, 569-582.

Miyamoto, D.T., Perlman, Z.E., Burbank, K.S., Groen, A.C., and Mitchison, T.J. (2004). The kinesin Eg5 drives poleward microtubule flux in Xenopus laevis egg extract spindles. J Cell Biol *167*, 813-818.

Muller-Reichert, T., Greenan, G., O'Toole, E., and Srayko, M. (2010). The elegans of spindle assembly. Cell Mol Life Sci *67*, 2195-2213.

Musacchio, A., and Desai, A. (2017). A Molecular View of Kinetochore Assembly and Function. Biology (Basel) *6*.

Nazockdast, E., and Redemann, S. (2020). Mechanics of the spindle apparatus. Seminars in cell & developmental biology.

Nehlig, A., Seiler, C., Steblyanko, Y., Dingli, F., Arras, G., Loew, D., Welburn, J., Prigent, C., Barisic, M., and Nahmias, C. (2020). Reciprocal regulation of Aurora kinase A and ATIP3 in the control of metaphase spindle length. Cell Mol Life Sci.

Nicklas, R.B. (1997). How cells get the right chromosomes. Science *275*, 632-637.

O'Toole, E.T., McDonald, K.L., Mantler, J., McIntosh, J.R., Hyman, A.A., and Muller-Reichert, T. (2003). Morphologically distinct microtubule ends in the mitotic centrosome of Caenorhabditis elegans. J Cell Biol *163*, 451-456.

Oegema, K., and Hyman, A.A. (2006). Cell division. WormBook : the online review of C elegans biology, 1-40.

Pereira, A.J., and Maiato, H. (2012). Maturation of the kinetochore-microtubule interface and the meaning of metaphase. Chromosome Res *20*, 563-577.

Petry, S. (2016). Mechanisms of Mitotic Spindle Assembly. Annu Rev Biochem *85*, 659-683.

Pintard, L., and Bowerman, B. (2019). Mitotic Cell Division in Caenorhabditis elegans. Genetics *211*, 35-73.

Powers, J., Rose, D.J., Saunders, A., Dunkelbarger, S., Strome, S., and Saxton, W.M. (2004). Loss of KLP-19 polar ejection force causes misorientation and missegregation of holocentric chromosomes. J Cell Biol *166*, 991-1001.

Praitis, V., Casey, E., Collar, D., and Austin, J. (2001). Creation of low-copy integrated transgenic lines in Caenorhabditis elegans. Genetics *157*, 1217-1226.

Quenouille, M.H. (1956). Notes on Bias in Estimation. Biometrika *43*.

Redemann, S., Baumgart, J., Lindow, N., Shelley, M., Nazockdast, E., Kratz, A., Prohaska, S., Brugues, J., Furthauer, S., and Muller-Reichert, T. (2017). C. elegans chromosomes connect to centrosomes by anchoring into the spindle network. Nat Commun *8*, 15288.

Riddle, D.L. (1997). C. elegans II (Plainview, N.Y.: Cold Spring Harbor Laboratory Press).

bioRxiv preprint doi: https://doi.org/10.1101/2022.11.07.515476; this version posted November 7, 2022. The copyright holder for this preprint (which was not certified by peer review) is the author/funder. All rights reserved. No reuse allowed without permission.

Risteski, P., Bozan, D., Jagric, M., Bosilj, A., Pavin, N., and Tolic, I.M. (2022). Length-dependent poleward flux of sister kinetochore fibers promotes chromosome alignment. Cell reports *40*, 111169.

Rueden, C., Schindelin, J., Hiner, M., and Eliceiri, K. (2021). SciJava Common. https://scijava.org/.

Sarov, M., Murray, J.I., Schanze, K., Pozniakovski, A., Niu, W., Angermann, K., Hasse, S., Rupprecht, M., Vinis, E., Tinney, M.*, et al.* (2012). A genome-scale resource for in vivo tag-based protein function exploration in C. elegans. Cell *150*, 855-866.

Saunders, A.M., Powers, J., Strome, S., and Saxton, W.M. (2007). Kinesin-5 acts as a brake in anaphase spindle elongation. Curr Biol *17*, R453-454.

Schechtman, E., and Wang, S. (2004). Jackknifing two-sample statistics. Journal of Statistical Planning and Inference *119*, 329-340.

Schindelin, J., Arganda-Carreras, I., Frise, E., Kaynig, V., Longair, M., Pietzsch, T., Preibisch, S., Rueden, C., Saalfeld, S., Schmid, B.*, et al.* (2012). Fiji: an open-source platform for biological-image analysis. Nat Methods *9*, 676-682.

Schneider, C.A., Rasband, W.S., and Eliceiri, K.W. (2012). NIH Image to ImageJ: 25 years of image analysis. Nat Methods *9*, 671-675.

Schneider, M.W.G., Gibson, B.A., Otsuka, S., Spicer, M.F.D., Petrovic, M., Blaukopf, C., Langer, C.C.H., Batty, P., Nagaraju, T., Doolittle, L.K.*, et al.* (2022). A mitotic chromatin phase transition prevents perforation by microtubules. Nature *609*, 183-190.

Schneider, M.W.G., Gibson, B.A., Otsuka, S., Spicer, M.F.D., Petrovic, M., Blaukopf, C., Langer, C.C.H., Doolittle, L.K., Rosen, M.K., and Gerlich, D.W. (2021). A chromatin phase transition protects mitotic chromosomes against microtubule perforation.

Sonnichsen, B., Koski, L.B., Walsh, A., Marschall, P., Neumann, B., Brehm, M., Alleaume, A.M., Artelt, J., Bettencourt, P., Cassin, E.*, et al.* (2005). Full-genome RNAi profiling of early embryogenesis in Caenorhabditis elegans. Nature *434*, 462-469.

Srayko, M., Kaya, A., Stamford, J., and Hyman, A.A. (2005). Identification and characterization of factors required for microtubule growth and nucleation in the early C. elegans embryo. Dev Cell *9*, 223-236.

Srayko, M., Quintin, S., Schwager, A., and Hyman, A.A. (2003). Caenorhabditis elegans TAC-1 and ZYG-9 form a complex that is essential for long astral and spindle microtubules. Curr Biol *13*, 1506-1511.

Steblyanko, Y., Rajendraprasad, G., Osswald, M., Eibes, S., Jacome, A., Geley, S., Pereira, A.J., Maiato, H., and Barisic, M. (2020). Microtubule poleward flux in human cells is driven by the coordinated action of four kinesins. EMBO J, e105432.

Steinmetz, M.O., and Prota, A.E. (2018). Microtubule-Targeting Agents: Strategies To Hijack the Cytoskeleton. Trends Cell Biol.

Sugioka, K., Fielmich, L.E., Mizumoto, K., Bowerman, B., van den Heuvel, S., Kimura, A., and Sawa, H. (2018). Tumor suppressor APC is an attenuator of spindle-pulling forces during C. elegans asymmetric cell division. Proc Natl Acad Sci U S A *115*, E954-E963.

Suzuki, A., Badger, B.L., Haase, J., Ohashi, T., Erickson, H.P., Salmon, E.D., and Bloom, K. (2016). How the kinetochore couples microtubule force and centromere stretch to move chromosomes. Nat Cell Biol *18*, 382-392.

bioRxiv preprint doi: https://doi.org/10.1101/2022.11.07.515476; this version posted November 7, 2022. The copyright holder for this preprint (which was not certified by peer review) is the author/funder. All rights reserved. No reuse allowed without permission.

Suzuki, A., Badger, B.L., and Salmon, E.D. (2015). A quantitative description of Ndc80 complex linkage to human kinetochores. Nat Commun *6*, 8161.

Tarailo, M., Kitagawa, R., and Rose, A.M. (2007). Suppressors of spindle checkpoint defect (such) mutants identify new mdf-1/MAD1 interactors in Caenorhabditis elegans. Genetics *175*, 1665-1679.

Timmons, L., and Fire, A. (1998). Specific interference by ingested dsRNA. Nature *395*, 854.

Tinevez, J.Y., Dragavon, J., Baba-Aissa, L., Roux, P., Perret, E., Canivet, A., Galy, V., and Shorte, S. (2012). A quantitative method for measuring phototoxicity of a live cell imaging microscope. Methods Enzymol *506*, 291-309.

Tinevez, J.Y., Perry, N., Schindelin, J., Hoopes, G.M., Reynolds, G.D., Laplantine, E., Bednarek, S.Y., Shorte, S.L., and Eliceiri, K.W. (2017). TrackMate: An open and extensible platform for single-particle tracking. Methods *115*, 80-90.

Uteng, M., Hentrich, C., Miura, K., Bieling, P., and Surrey, T. (2008). Poleward transport of Eg5 by dynein-dynactin in Xenopus laevis egg extract spindles. J Cell Biol *182*, 715-726.

Vicente, J.J., and Wordeman, L. (2019). The quantification and regulation of microtubule dynamics in the mitotic spindle. Curr Opin Cell Biol *60*, 36-43.

Wandke, C., Barisic, M., Sigl, R., Rauch, V., Wolf, F., Amaro, A.C., Tan, C.H., Pereira, A.J., Kutay, U., Maiato, H.*, et al.* (2012). Human chromokinesins promote chromosome congression and spindle microtubule dynamics during mitosis. J Cell Biol *198*, 847-863.

Waters, J.C., Mitchison, T.J., Rieder, C.L., and Salmon, E.D. (1996). The kinetochore microtubule minus-end disassembly associated with poleward flux produces a force that can do work. Mol Biol Cell *7*, 1547-1558.

White, J., and Stelzer, E. (1999). Photobleaching GFP reveals protein dynamics inside live cells. Trends Cell Biol *9*, 61-65.

Wolff, I.D., Hollis, J.A., and Wignall, S.M. (2021). Acentrosomal spindle assembly and stability in C. elegans oocytes requires a kinesin-12 non-motor microtubule interaction domain.

Woodruff, J.B., Wueseke, O., Viscardi, V., Mahamid, J., Ochoa, S.D., Bunkenborg, J., Widlund, P.O., Pozniakovsky, A., Zanin, E., Bahmanyar, S.*, et al.* (2015). Centrosomes. Regulated assembly of a supramolecular centrosome scaffold in vitro. Science *348*, 808-812.

Wordeman, L., and Vicente, J.J. (2021). Microtubule Targeting Agents in Disease: Classic Drugs, Novel Roles. Cancers (Basel) *13*.

Wordeman, L., Wagenbach, M., and von Dassow, G. (2007). MCAK facilitates chromosome movement by promoting kinetochore microtubule turnover. J Cell Biol *179*, 869-879.

Yang, G., Cameron, L.A., Maddox, P.S., Salmon, E.D., and Danuser, G. (2008). Regional variation of microtubule flux reveals microtubule organization in the metaphase meiotic spindle. J Cell Biol *182*, 631-639.

Ye, A.A., Cane, S., and Maresca, T.J. (2016). Chromosome biorientation produces hundreds of piconewtons at a metazoan kinetochore. Nat Commun *7*, 13221.

Zelinski, B., Muller, N., and Kierfeld, J. (2012). Dynamics and length distribution of microtubules under force and confinement. Phys Rev E Stat Nonlin Soft Matter Phys *86*, 041918.

Zhai, Y., Kronebusch, P.J., and Borisy, G.G. (1995). Kinetochore microtubule dynamics and the metaphase-anaphase transition. J Cell Biol *131*, 721-734.

bioRxiv preprint doi: https://doi.org/10.1101/2022.11.07.515476; this version posted November 7, 2022. The copyright holder for this preprint (which was not certified by peer review) is the author/funder. All rights reserved. No reuse allowed without permission.

Zhang, D., Rogers, G.C., Buster, D.W., and Sharp, D.J. (2007). Three microtubule severing enzymes contribute to the "Pacman-flux" machinery that moves chromosomes. J Cell Biol *177*, 231-242.